Thermodynamic modeling of the Nb-Ni system with uncertainty quantification using PyCalphad and ESPEI

Hui Sun[a], Shun-Li Shang[a], Rushi Gong[a], Brandon J. Bocklund[a, b], Allison M. Beese[a, c],

and Zi-Kui Liu[a]

[a] Department of Materials Science and Engineering, The Pennsylvania State University,

University Park, PA, 16802, USA

[b] Lawrence Livermore National Laboratory, Livermore, CA 94550, USA

[c] Department of Mechanical Engineering, Pennsylvania State University,

University Park, PA 16802, United States

Abstract: The Nb-Ni system is remodeled with uncertainty quantification (UQ) using software tools of PyCalphad and ESPEI (the Extensible, Self-optimizing Phase Equilibria Infrastructure) with the presently implemented capability of modeling site occupancy based on Wyckoff positions. The five- and three-sublattice models are used to model the topologically close pack (TCP) μ-Nb_7Ni_6 and δ-$NbNi_3$ phases according to their Wyckoff positions. The inputs for CALPHAD-based thermodynamic modeling include the thermochemical data as a function of temperature predicted by first-principles and phonon calculations based on density functional theory (DFT), ab initio molecular dynamics (AIMD) simulations, together with phase equilibrium and site occupancy data in the literature. In addition to phase diagram and thermodynamic properties, the CALPHAD-based predictions of site occupancies of Nb in μ-Nb_7Ni_6 agree well with experimental data. Furthermore, the UQ estimation using the Markov Chain Monte Carlo (MCMC) method as implemented in ESPEI is applied to study the uncertainty of site occupancy in μ-Nb_7Ni_6 and enthalpy of mixing (ΔH_{mix}) in liquid.

Highlights

- New capability implemented into PyCalphad and ESPEI to model site occupancy
- TCP phases (μ-Nb_7Ni_6 and δ-$NbNi_3$) modeled using sublattice models according to their Wyckoff positions
- Finite-temperature thermochemical properties predicted by DFT-based first-principles and phonon calculations
- Energetics of the Nb-Ni liquid phase predicted by AIMD simulations
- Uncertainty quantification of model parameters and calculations

Keywords: CALPHAD modeling; Nb-Ni; PyCalphad and ESPEI; First-principles and phonon calculations; AIMD simulations; Site occupancy; TCP phases; Uncertainty quantification.

1. Introduction

Topologically close pack (TCP) phases, also known as the Frank-Kasper phases [1], are intermetallic compounds with complex crystalline structures, and are frequently observed in Ni-based superalloys, for example, the $\sigma, \chi, P, R, \delta, \mu, M$, A15, and Laves phases [2]. TCP phases are usually brittle and detrimental, and hence, understanding their phase stability is of great importance for improving the performance of Ni-based superalloys [3]. For instance, when Ni-based superalloys are highly alloyed with refractory elements (e.g., Cr, Mo, Nb, Ta, W, and Re) to achieve better strengths at high temperatures, TCP phases may form and drain refractory elements from the matrix to reduce the solid solution strengthening in the FCC-based γ phase in Ni-based superalloys [4] or the formation of the strengthening phase like the $L1_2$-based γ' phase in Co-based superalloys [5].

In the present work, the TCP phases in the Nb-Ni system, i.e., δ-$NbNi_3$ and μ-Nb_7Ni_6, are investigated. They drain alloying element Nb from the matrix [6] and are deleterious to the performance of Ni-based superalloys. For example, the formation of a 10% volume fraction of δ-$NbNi_3$ can lower the elongation of Inconel 718 by 40% [7], and the formation of around 10 vol.% of δ-$NbNi_3$ after stress relief heat treatment resulted in a 45% reduction of the fracture strain in Inconel 625 [8]. Similarly, μ-Nb_7Ni_6 shows an undesirable influence on mechanical properties, for example, the precipitation in the Ni-Mo-Cr alloy decreased its room temperature impact roughness by 100 J in the Charpy test [9]. Therefore, a better understanding concerning the formation of TCP phases is desirable and can be accomplished through accurate thermodynamic modeling based on the CALPHAD approach aided by first-principles, phonon calculations, and ab initio molecular dynamics (AIMD) simulations based on density functional theory (DFT) [10].

The TCP phase δ-$NbNi_3$ consists of three Wyckoff sites (2a, 2b, and 4e) with space group *Pmmn* (No. 59) [11], and the TCP phase μ-Nb_7Ni_6 has five Wyckoff sites (3a, 6c(1), 6c(2), 6c(3), and 18h) with space group $R\bar{3}m$ (No. 166) [12]; see details in Table 1. The crystallographic information of Wyckoff sites indicates that a three-sublattice model is needed for a complete description of δ-$NbNi_3$ and a five-sublattice model for μ-Nb_7Ni_6, respectively [13,14]. However, previous CALPHAD modeling of the Nb-Ni system [15–19] used models with fewer sublattices, which cannot capture well their site occupancies. For example, μ-Nb_7Ni_6 was described by $(Ni)_{0.47}(Nb)_{0.53}$ [15], $(Nb, Ni)_7(Nb)_6$ [16], and $(Nb, Ni)_1Ni_4(Nb, Ni)_2Nb_6$ [18] as shown in Table 2, and the Nb occupancies in various Wyckoff sites of μ-Nb_7Ni_6 measured by Joubert et al. [20] can thus not be reproduced. While Joubert et al. [21] adopted a five-sublattice model for μ-Nb_7Ni_6, i.e., $(Nb, Ni)_1Nb_2Nb_2(Nb, Ni)_2(Nb, Ni)_6$, with a better description of solubility and site occupancy. Two of the sublattices in their model [21] include only Nb, which may limit its extension to higher order systems. Most recently, Chen et al. [17] and Zhou et al. [19] remodeled the Nb-Ni system with the $(Nb, Ni)_1Nb_4(Nb, Ni)_2(Nb, Ni)_6$ model for μ-Nb_7Ni_6 and the $(Nb, Ni)_3(Nb, Ni)_1$ model for δ-$NbNi_3$, but assigned an arbitrary value of 5000 J/mol-atom as the enthalpy of formation (ΔH_{form}) for a number of endmembers of the TCP phases with one element in each Wyckoff site.

The present work aims to remodel the Nb-Ni system in terms of the CALPHAD approach using the open-source tools of ESPEI (the Extensible, Self-optimizing Phase Equilibria Infrastructure) [22,23], where the PyCalphad [24,25] is the computing engine for thermodynamic calculations. The sublattice models for both δ-$NbNi_3$ and μ-Nb_7Ni_6 are based on their three and five Wyckoff sites, respectively, and free energies of all endmembers in the sublattice models are predicted by

DFT-based first-principles and phonon calculations, as well as machine learning (ML). The short-range order as well as enthalpy of mixing in liquid phase is predicted by AIMD simulations. In ESPEI, the model parameters of individual phases are first evaluated from single-phase thermochemical data and then refined using the Markov Chain Monte Carlo (MCMC) method based on experimental site occupancy and phase equilibrium data in the literature. The MCMC method further enables uncertainty quantification (UQ). It is noted that the new capability to use site occupancies as input data for evaluating model parameters in ESPEI is implemented in the present work.

2. Overview of previous CALPHAD modeling

There are six phases in the Nb-Ni system, i.e., three solution phases (BCC, FCC, and liquid) and three intermetallic compounds (μ-Nb_7Ni_6, δ-$NbNi_3$, and $NbNi_8$) as summarized by Chen et al. [17]. Among various modeling works (see Table 2) [15–19], Kaufman and Nesor [15] considered μ-Nb_7Ni_6 and δ-$NbNi_3$ as stoichiometric compounds by omitting the Nb solubilities in these two phases [26–28] for simplification. Zeng et al. [18] adopted the model of $(Nb, Ni)_1Ni_4(Nb, Ni)_2Nb_6$ for μ-Nb_7Ni_6, but could not reproduce well the solubilities of Nb in the composition range of 50 – 54 at. % Nb around 1100℃ measured by Duerden et al. [27] and the enthalpies of formation measured by Argent et al. [29] with a large discrepancy around 13 kJ/mol-atom. Bolcavage and Kattner [16] did not consider $NbNi_8$ due to the lack of experimental data at that time, and the calculated liquidus in the Nb-rich region around 200 – 300 K was higher than the experimental data by Wicker et al. [30]. Joubert et al. [21] used a common default value of 5000 J/mol-atom to describe the ΔH_{form} for some endmembers in the TCP phases, resulting in a less accurate modeling of site occupancies in μ-Nb_7Ni_6 in comparison with their earlier experimental data [20].

The most recent modeling work by Chen et al. [17] is used in thermodynamic modeling of ternary systems such as Fe-Nb-Ni [31], Nb-Ni-Zr [32], and Nb-Ni-Ti [33]. However, phase boundaries between μ-Nb_7Ni_6 and δ-$NbNi_3$ and between μ-Nb_7Ni_6 and BCC are not reproduced satisfactorily in comparison with the measurements by Murametsu et al. [26]. Chen et al. [17] did not incorporate the experimental temperatures of liquid with respect to BCC, which were measured by Wicker et al. [30]. This was because the differential thermal analysis (DTA) of 60 at. % Nb at 1723 K did not observe the formation of liquid phase [28]. Additionally, the enthalpies of mixing for liquid at 1823 K by Chistyakov et al. [34] were not considered due to their inconsistency with the data from Schaefers et al. [35]. The modeling by Zhou et al. [19] considered the enthalpies of mixing for liquid at 1823 K measured by Chistyakov et al. [34] and Sudavtsova et al. [36]. However, Zhou et al. [19] neglected the temperatures of liquidus measured by Wicker et al. [30].

In the present work, the sublattice models of $(Nb, Ni)_1(Nb, Ni)_1(Nb, Ni)_2$ and $(Nb, Ni)_1(Nb, Ni)_2(Nb, Ni)_2(Nb, Ni)_2(Nb, Ni)_6$ are adopted to model δ-$NbNi_3$ and μ-Nb_7Ni_6 as shown in Table 3, corresponding to their Wyckoff positions presented in Table 1.

3. Literature review of phase equilibrium and thermochemical data

3.1. Phase equilibrium data

Phase boundaries between FCC and liquid (0 – 15 at. % Nb) were measured by Duerden et al. [27], Pogodin et al. [37] , and Grube et al. [38] using thermal analysis via heating curves, by Chen et al. [28] and Kajikawa [39] using differential thermal analysis (DTA), and by Kajikawa [39] using the solid-liquid diffusion couple method (DCM). All these measurements show a good agreement with each other with the temperature variation at each fixed composition less than 40 K and are used in the present CALPHAD modeling of the Nb-Ni system.

Phase boundaries between FCC and δ-$NbNi_3$ (0 – 15 at. % Nb) were measured by Pogodin et al. [37] and Grube et al. [38] using thermal analysis from heating curves. Guseva et al. [40] detected the FCC to δ-$NbNi_3$ transition using X-ray powder diffraction (XRD) at 1073 – 1473 K. Joubert et al. [21] measured the homogeneity range of δ-$NbNi_3$ using electron probe micro-analysis (EPMA). Chen et al. [28] attempted to use DFT-based calculation to estimate the FCC to δ-$NbNi_3$ transition at 1322 K. All these measurements show a good agreement with each other with the composition variation about 5 at. % Nb from 1000 K to 1500 K and are used in the present CALPHAD modeling.

The $NbNi_8$ phase was observed by Quist et al. [41] using transmission electron microscopy (TEM) and confirmed by Joubert et al. [21] by examining samples annealed at 723 K for 76 days using XRD. Wekken et al. [42] detected the existence of $NbNi_8$ through changes in electrical resistivity, showing that $NbNi_8$ forms at 10.3 at. % Nb at 853 K. Chen et al. [28] observed $NbNi_8$ with differential scanning calorimetry (DSC). Therefore, $NbNi_8$ is considered as a stable phase in the present work.

The Nb_2Ni phase was observed by Zhao et al. [43] using TEM in a sample annealing at 1523 K for 5h. However, this phase was not confirmed further by using samples with a longer annealing time. The formation energy of Nb_2Ni is -0.041 eV/atom (-3.96 kJ/atom), which is above the convex hull (-19.43 kJ/atom at 66.7 at. % Nb) as shown in Fig. 1. The Nb_2Ni phase is hence excluded in the present modeling work.

Regarding the solubility range of δ-$NbNi_3$, Murametsu et al. [26] observed 24.0 – 26.6 at. % Nb in the temperature range of 1023 K – 1303 K by EPMA. Chen et al. [28] reported the phase boundary between 23.4 – 25.7 at. % Nb by DTA at 1323 K for 336h. Duerden et al. [27] estimated the phase boundary around 23.5 – 26.5 at. % Nb at 1273 K using XRD. The phase boundaries of δ-$NbNi_3$ between δ-$NbNi_3$ and liquid were measured by Grube et al. [38], Duerden et al. [20], and Svechnikov et al. [44] using heating curves of thermal analysis, and by Chen et al. [28] using DTA. All these data are consistent with each other and hence are considered in the present CALPHAD modeling.

For the solubility range of μ-Nb_7Ni_6, Duerden et al. [27] estimated 50 – 54 at. % Nb at 1373 K using optical microscopy. Svechnikov et al. [44] reported 49.8 - 58.3 at. % Nb by means of the heating curves of thermal analysis. Murametsu et al. [26] measured the values of 48.6 - 56.2 at. % Nb around 1023 K – 1303 K by EPMA. Joubert et al. [20] reported 49.6 - 56.9 at. % Nb at 1273 K by EPMA. Chen et al. [28] estimated 49.5 – 56.3 at. % Nb around 1273 K – 1303 K by EPMA. The phase boundaries between μ-Nb_7Ni_6 and liquid were measured by Duerden et al. [27] and Svechnikov et al. [44] using the heating curves of thermal analysis and by Chen et al. [28] using

DTA. All these data are in reasonable agreement with each other and hence are included in the present CALPHAD modeling.

The temperatures of invariant reactions between liquid, δ-$NbNi_3$, and FCC phases agree well with each other from 1170 K to 1175 K by Chen et al. [28] using DTA, and by Duerden et al. [28] and Svechnikov et al. [45] using the heating curves of thermal analysis. At the same time, the invariant temperatures between liquid, δ-$NbNi_3$, and μ-Nb_7Ni_6 phases have a difference of 30 K (from 1290 to 1320 K) measured by Duerden et al. [28] and Wicker et al. [30]. Nevertheless, all these data are included in the present CALPHAD modeling.

The phase boundaries between liquid and BCC were measured by Svechnikov et al. [45] and Wicker et al. [30] by quenching the samples, and by Duerden et al. [27] by heating, cooling, and quenching the samples. Chen et al.'s modeling work did not consider the data from Wicker et al. [30] because the new DTA experiment from Chen et al. [28] did not observe any phase transformation at 60 at. % Nb. While these measurements exhibit noticeable discrepancies, as much as 300 K, the present modeling work considers all these experimental data, but lower weights were given to the data from Wicker et al. [30].

3.2. Thermochemical data

Enthalpies of formation for the Nb-Ni system were measured by Argent et al. [29] through the calorimetry method from 12.5 – 75.0 at. % Nb with an estimated error around 4 kJ/mol-atom. Sokolvskaya et al. [36], Alekseev et al. [46], and Lyakishev et al. [47] used the electromotive force (emf) method to determine the enthalpies of formation for intermediate phases with 25.0 and 50.0

at. % Nb. However, as shown in Fig. 1. the results from Alekseev et al. [46] and Sokolvskaya et al. [36] show great discrepancies around 8 kJ/mole-atom at 25.0 at. % Nb with respect to those from Argent et al. [29] Furthermore, the DFT-based results using the generalized gradient approximation (GGA) from the Materials Project [48] and the Open Quantum Materials Database (OQMD) [49] are included in Fig. 1 and are about 10% less negative than experimental data; agreeing with the general trends between DFT results and experimental data [50]. At the same time, DFT calculations from the present work (see detailed methodology later) are also shown in Fig. 1, including all endmembers for both μ-Nb_7Ni_6 (32 points) and δ-$NbNi_3$ (8 points). The DFT calculations from the present work agree with the DFT results from the Materials Project [48] and the OQMD [49] at the compositions of 25.0 at. % Nb and 53.3 at. % Nb. The data from Argent et al. [29] are closer to the results from DFT-based predictions than those from Sokolvskaya et al. [36] and hence adopted in the present CALPHAD modeling.

Two sets of values about enthalpy of mixing, ΔH_{mix}, were reported for the Ni-rich liquid as shown in Fig. 2. The values from Schaefers et al. [35] at 1927 K and 2000 K show a larger difference (e.g., around 15 kJ/mol-atom at 30.0 at. % Nb) compared with those from Chistyakov et al. [34] at 1823 K and Sudavtsova et al. [36] at 1927 K. In general, the enthalpies for liquids and solids should be compatible with each other in the same alloy system. For example, in the Al-Cu system [51] the difference between ΔH_{mix} in liquid and the ΔH_{form} in solid is around 4 kJ/mole-atom at 40.0 – 60.0 at. % Cu, and in the Fe-Ni system [52] the difference is around 5 kJ/mole-atom at 50.0 – 75.0 at. % Ni. The enthalpies of formation of solids in the Nb-Ni system are around 30 kJ/mole-atom at 25.0 at. % Nb, which is closer to the data of liquid (around 25 kJ/mole-atom) measured by Chistyakov et al. [34] and Sudavtsova et al. [36]. At the same time, AIMD is employed in the present work to predict ΔH_{mix} of liquid at 2700 K (see details later, the results are 17.90 kJ/mole-atom at 11.1 at. % Nb, 20.15 at 22.2 at. % Nb, 26.73 at 33.3 at. % Nb, 21.72 at 50.0 at. % Nb). The present AIMD results at 2700 K are much closer to the values from Chistyakov et al. [34] at 1823 K and Sudavtsova et al. [36] at 1927 K, which are adopted in the present CALPHAD modeling.

The site occupancy data are only available for Nb in μ-Nb_7Ni_6 at 1273 K measured by Joubert et al. [20] using EPMA. With the present implementation of the ESPEI code (see details in Sec. 4.3.2), these data are included in the present CALPHAD modeling.

4. Methodology

4.1. DFT-based first-principles calculations

DFT-based first-principles calculations can predict Helmholtz energy of solid phase as a function of temperature and volume. The expression for Helmholtz energy (i.e., the Gibbs energy under zero external pressure) within the quasiharmonic approach is [53],

$$F(V,T) = E_0(V) + F_{vib}(V,T) + F_{el}(V,T) \qquad \text{Eq. 1}$$

where F is the Helmholtz energy, T the absolute temperature, V the volume, $E_0(V)$ the static energy at 0 K without vibrational contribution, F_{vib} the contribution from lattice vibrations, and F_{el} the contribution from thermal electrons. The equilibrium volume at each T was obtained by searching $P = -\frac{\partial F}{\partial V} = 0$.

The energy versus volume (E-V) curve for each phase (or endmember) at 0 K was predicted by DFT-based calculations at 7 volumes and fitted by the following 4-parameter Birch-Murnaghan (BM4) equation of state (EOS) [53],

$$E_0(V) = k_1 + k_2 V^{-2/3} + k_3 V^{-4/3} + k_4 V^{-2} \qquad \text{Eq. 2}$$

where k_1, k_2, k_3, and k_4 are fitting parameters. This EOS contains four equilibrium properties at $P = 0$ GPa, i.e., the equilibrium energy E_0, volume V_0, bulk modulus B_0, and the pressure derivative of bulk modulus B'. The vibrational contribution F_{vib} was obtained by the phonon density of states (pDOS) [54],

$$F_{\text{vib}}(T, V) = k_B T \int_0^{\infty} \ln\left[2 \sinh \frac{\hbar\omega}{2k_B T}\right] g(\omega)\, d\omega \qquad \text{Eq. 3}$$

where $g(\omega)$ is the pDOS as a function of V and frequency ω. The thermal electronic contribution F_{el} was obtained from Mermin statistics through $F_{el} = E_{el} - TS_{el}$, where E_{el} was the internal energy and S_{el} the bare electronic entropy [54].

DFT-based first-principles calculations were performed for the two reference elements of BCC-Nb and ferromagnetic (FM) FCC-Ni and two TCP phases of δ-$NbNi_3$ and μ-Nb_7Ni_6. δ-$NbNi_3$ was modeled by a three-sublattice model with a total of 8 endmembers; and μ-Nb_7Ni_6 was modeled by a five-sublattice model with 32 endmembers; see details in Table 2. Phonon calculations were performed for BCC-Nb, FCC-Ni, and the selected endmembers of δ-$NbNi_3$ and μ-Nb_7Ni_6 with negative values of enthalpy of formation, including $Nb_2Ni_2Ni_4$ and $Ni_2Nb_2Ni_4$ for δ-$NbNi_3$, and $Nb_6Nb_6Nb_6Ni_{18}Nb_3$, $Nb_6Nb_6Nb_6Ni_{18}Ni_3$, $Nb_6Nb_6Ni_6Ni_{18}Ni_3$, and $Nb_6Ni_6Nb_6Ni_{18}Nb_3$ for μ-Nb_7Ni_6. Note that the scattered E-V datapoints resulting in unreliable properties by EOS fitting especially B_0 and B', the Debye model to estimate thermodynamic properties is hence not applied herein for the non-stable endmembers.

The Vienna *ab initio* Simulation Package (VASP) [55] was used for DFT-based first-principles, phonon, and AIMD simulations in the present work. The projector augmented wave (PAW) method was used to describe the ion-electron interaction [56], while the generalized gradient approximation (GGA) by Perdew, Burke, and Ernzerhof (PBE) was used to describe the exchange-correlation functional [57]. The NVT ensemble (fixed total number of atoms (N) in the 108-atom supercell and fixed V and T) is used during AIMD simulations, while the Nose-Hoover thermostat was adopted to control the temperature [58,59].The plane-wave cutoff energy was set to be 368 eV for structural relaxations and phonon calculations, and 520 eV for the final static calculations to get accurate E-V data points and electron DOS's. The convergence criterion of electronic self-consistency was set as 6×10^{-5} eV/atom for structural relaxations, static calculations, and phonon calculations. The details of DFT-based first-principles, phonon calculations, and AIMD for each compound or element, including total atom(s) in the cell for the calculations, *k*-points meshes for structure relaxations and the final static calculations (indicated by DFT), supercell sizes for phonon calculations, *k*-points meshes for phonon calculations, and *k*-points meshes for AIMD calculations are summarized in Table 4. The selected electronic configurations were $4p^64d^45s^1$ and $3p^63d^64s^2$ for Nb and Ni, respectively, which are the same as those used by the Materials Project [48] along with the same crystal structure files for VASP calculations. AIMD simulations were performed in a cubic supercell with 108 atoms at six compositions (Ni_{108}, $Nb_{12}Ni_{96}$, $Nb_{24}Ni_{84}$, $Nb_{36}Ni_{72}$, $Nb_{54}Ni_{54}$, and Nb_{108}). A single Γ point 1×1×1 was chosen as the *k*-point mesh, and the 280 eV was set as cutoff energy. The 2700 K was adopted for AIMD simulations to ensure that all the six compositions are in the liquid state.

ML was also applied to provide both the phase equilibrium data and thermochemical data [60–62]. Here, the stable configurations of μ-Nb_7Ni_6 were predicted by ML and verified by DFT calculations as shown in Fig. 3. The stable configurations predicted by ML code of Alignn [61] contained 4 out of 5 stable configurations from DFT calculations, while SIPFENN [62] included 2 out of 5 stable configurations from DFT calculations. Two types of ML predictions of enthalpy of formation were adopted here, i.e., using the light model from SIPFENN [62] and the model from Alignn [61]. SIPFENN [62] is an ML tool to predict enthalpy of formation by using structural files including atomic species and crystallographic information. The light model in SIPFENN [62] was trained based on OQMD data [49,63] with the mean absolute error (MAE) of 41.9 meV/atom. Similarly, the enthalpy of formation from Alignn [61] also only requires structural files, but Alignn [61] was trained based on the properties from JARVIS (Joint Automated Repository for Various Integrated Simulations) [64] with the MAE of 26.06 meV/atom.

4.2. CALPHAD modeling

4.2.1. Thermodynamic models

There are three types of phases in the Nb-Ni system, i.e., the solution phases of BCC, FCC, and liquid, the stoichiometric compound of $NbNi_8$, and the non-stoichiometric TCP phases of δ-$NbNi_3$ and μ-Nb_7Ni_6. For the solution phases, the Redlich-Kister polynomial [65] was adopted to describe Gibbs energy,

$$G_m^\alpha = x_{Nb}G_{Nb}^\alpha + x_{Ni}G_{Ni}^\alpha + RT(x_{Nb}lnx_{Nb} + x_{Ni}lnx_{Ni}) + x_{Nb}x_{Ni}\sum_{k=0} {}^kL_{Nb,Ni}^\alpha(x_{Nb} - x_{Ni})^k \qquad \text{Eq. 3}$$

where x_{Nb} and x_{Ni} are the mole fractions of Nb and Ni in phase α. G_{Nb}^{α} and G_{Ni}^{α} are the Gibbs energies of pure Nb and pure Ni in phase α with respect to their standard element reference (SER) states at P = 1 bar and T = 298.15 K, taken from the Scientific Group Thermodata Europe (SGTE) database [66]. R is the gas constant, T is the temperature, and ${}^{k}L_{Nb,Ni}$ is the kth interaction parameter between Nb and Ni,

$$ {}^{k}L_{Nb,Ni}^{\alpha} = a + bT \qquad \text{Eq. 4} $$

where a and b are model parameters.

NbNi$_8$ was treated as a stoichiometric compound with its Gibbs energy described by,

$$ G_{Nb:Ni}^{NbNi_8} = {}^{0}G_{Nb}^{BCC} + 8\,{}^{0}G_{Ni}^{FCC} + A + BT \qquad \text{Eq. 5} $$

where A and B are model parameters. ${}^{0}G_{Nb}^{BCC}$ and ${}^{0}G_{Ni}^{FCC}$ are the Gibbs energies of pure Nb and pure Ni in their stable structures, i.e., BCC and FCC, respectively. The values of ${}^{0}G_{Nb}^{BCC}$ and ${}^{0}G_{Ni}^{FCC}$ were taken from the SGTE database [66].

For the non-stoichiometric compounds, the compound energy formalism (CEF) [14] was used to describe the phase with its sublattices corresponding to its Wyckoff sites, see Table 1. In the CEF, the Gibbs energy in per mole of formula (mf) is described as follows [67],

$$ G_{mf} = {}^{0}G_{mf} + RT\sum_{t} a^{t} \sum_{i} y_{i}^{t} ln y_{i}^{t} + {}^{E}G_{mf} \qquad \text{Eq. 6} $$

where ${}^{0}G_{mf}$ denotes the Gibbs energy contribution of all endmembers, which can be calculated by summation of the product of site fraction (y_{i}^{t}) of each component (i) in its sublattice and the Gibbs energy of the corresponding endmember (${}^{0}G_{em}$)

$$ {}^{0}G_{mf} = \sum_{em} \left(\prod_{t} y_i^t \ {}^{0}G_{em} \right) \quad \text{Eq. 7} $$

$\sum_t a^t \sum_i y_i^t ln y_i^t$ is the sublattice ratio a^t (in the sublattice t) times the ideal mixing in this sublattice, where the ideal mixing is calculated by the site fraction y_i^t and the natural logarithm of site fraction y_i^t . ${}^{E}G_{mf}$ is the excess Gibbs energy which contains the contributions from the mixing in one sublattice where all other sublattices only contain one component each; and from the mixing in more than one sublattice where more than one sublattices contain two or more components. Here only the first type interaction between components Nb and Ni is considered, calculated by the summation of energy of all sublattice t that can be occupied by two components (i and j) with the other sublattices (s) containing only one component as follows

$$ {}^{E}G_{mf} = \sum_{t} \prod_{s \neq t} y_l^s \sum_{i>j} \sum_{j} y_i^t \, y_j^t \, L_{i,j:l}^t \quad \text{Eq. 8} $$

4.2.2. Evaluation of model parameters using ESPEI

The open-source software tools, PyCalphad [24,25] and ESPEI [22,23], were employed in the present work to remodel the Nb-Ni system. PyCalphad is a Python-based code on thermodynamic calculations for a wide range of thermodynamic models. ESPEI is a tool for the evaluation of model parameters using PyCalphad as the computational engine to perform thermodynamic calculations. ESPEI works in two steps: first, choose and evaluate model parameters of individual phases using thermochemical data, and second, optimize model parameters and quantify uncertainties of model parameters using both thermochemical and phase equilibrium data through Bayesian parameter estimation via an ensemble MCMC [68–70].

Since the site occupancy data could not be used as input for CALPHAD modeling in the previous version of ESPEI, a new function was hence implemented to add site occupancy data as input for the evaluation of model parameters and their uncertainties. In the Bayesian parameter estimation, the acceptance of parameters is based on the posterior probability $p(\theta/D)$ of the model parameters θ under the data D, which is calculated by the likelihood $p(D/\theta)$, the prior $p(\theta)$, and the evidence $p(D)$, i.e., $p(\theta/D) = p(D/\theta) * p(\theta)/p(D)$. The likelihood $p(D/\theta)$ is related to how well experimental data are described by the proposed parameters, and the prior $p(\theta)$ is the probability distribution of each parameter. The flowchart of the present implementation of site occupancies as input data for ESPEI is illustrated in Fig. 4, including the new JavaScript Object Notation (JSON) data format for site occupancies, new model parameter values evaluated from the MCMC method, and the log-type posterior probabilities calculated from the prior and likelihood of site occupancy and other experimental data. The acceptance of the new parameters is determined by the Metropolis-Hastings criteria [70], comparing the posterior probabilities calculated from the new parameters with those from the current parameters. To be consistent with the weighting of errors from different types of data, the likelihood for site occupancy data is normalized by the standard deviation of error which is set to be 0.01 using Gaussian distribution. In the present work, experimental data of site occupancy by Joubert et al. [20] were used to remodel μ-Nb_7Ni_6 as discussed in Sec. 4.3.

Uncertainty quantification (UQ) in ESPEI uses the samples from different Markov chains in the MCMC optimizations to estimate the uncertainties of thermodynamic properties [71]. In the present work, the UQ of site occupancy is implemented in ESPEI, and four chains for each parameter were used with 1000 MCMC steps.

5. Results and discussion

5.1. Thermodynamic properties by first-principles calculations

Table 5 summarizes the space group and the predicted properties of V_0, B_0, and B'_0 for BCC-Nb, FCC-Ni, δ-$NbNi_3$ ($Ni_1Nb_1Ni_2$), and μ-Nb_7Ni_6 ($Nb_2Nb_2Nb_2Ni_6Ni_1$) at 0 and 273 K, in comparison with available experimental data [11,12,72,73]. It shows that the B_0 values from DFT-based predictions differ from experimental data by 1.0% for BCC-Nb and 5.0% for FCC-Ni, respectively [72,73]. Table 5 shows that V_0 increases from BCC-Nb, μ-Nb_7Ni_6, FCC-Ni, to δ-$NbNi_3$ with the difference between DFT-based calculations and experiments being about 1.72%. δ-$NbNi_3$ has the highest bulk modulus (207.7 GPa), followed by μ-Nb_7Ni_6 (200.0 GPa), FCC-Ni (195.9 GPa), and BCC-Nb (173.5 GPa), indicating that the bonding in δ-$NbNi_3$ is the strongest. The B' values increase from BCC-Nb (3.86), μ-Nb_7Ni_6 (4.48), δ-$NbNi_3$ (4.65), to FCC-Ni (4.81), indicating the increase of the thermal expansion coefficient from Nb (7.1×10^{-6} K^{-1}) to Ni (12.8×10^{-6} K^{-1}) [74].

Fig. 5 shows the predicted entropy and enthalpy of BCC-Nb as a function of temperature from the present DFT calculations using Eq. 1, with an average difference of 4.83% and 5.79% and the standard deviation of 0.49 and 0.97 for entropy and enthalpy in comparison with the superimposed SGTE data [66]. Similarly, Fig. 6 presents the predicted entropy and enthalpy of FCC-Ni as a function of temperature from the present DFT calculations using Eq. 1, showing a good agreement with the SGTE database [66] with an average difference of 3.24% and 6.44% and a standard deviation of 1.21 and 2.42 for entropy and enthalpy, respectively. Table 6 exhibits the ΔH_{form} of δ-$NbNi_3$ ($Ni_1Nb_1Ni_2$) and μ-Nb_7Ni_6 ($Nb_2Nb_2Nb_2Ni_6Ni_1$ and $Nb_2Nb_2Nb_2Ni_6Nb_1$) predicted from

DFT-based first-principles calculations at 0 K and phonon calculations at room temperature and compared with experimental data [29]. The configurations on the convex hull around the compositions of 25 at. % Nb and 50 at. % Nb are chosen to represent the ΔH_{form} for δ-$NbNi_3$ ($Ni_1Nb_1Ni_2$) and μ-Nb_7Ni_6 ($Nb_2Nb_2Nb_2Ni_6Ni_1$ and $Nb_2Nb_2Nb_2Ni_6Nb_1$). The predicted ΔH_{form} value of δ-$NbNi_3$ ($Ni_1Nb_1Ni_2$) is -28.38 kJ/mol-atom at 0 K (and -28.51 kJ/mol-atom at room temperature). The difference between the predicted ΔH_{form} value and the experimental result (-31.8 kJ/mol-atom) is 3.33 kJ/mol-atom at 0 K (and 3.20 kJ/mol-atom at room temperature), which is less than the reported error (4.02 kJ/mol-atom) measured by Argent et al. [29] using the calorimetry method for three samples at 25 at. % Nb. While the predicted ΔH_{form} value of μ-Nb_7Ni_6 ($Nb_2Nb_2Nb_2Ni_6Ni_1$) is -20.63 kJ/mol-atom at 0 K (and -20.38 kJ/mol-atom at room temperature). At the same time, the predicted ΔH_{form} value of μ-Nb_7Ni_6 ($Nb_2Nb_2Nb_2Ni_6Nb_1$) is -20.50 kJ/mol-atom at 0 K (and -20.43 kJ/mol-atom at room temperature). The difference between the predicted ΔH_{form} value for 50 at. % Nb of μ-Nb_7Ni_6 (-20.56 kJ/mol-atom at 0 K and -20.41 kJ/mol-atom at room temperature by averaging ΔH_{form} values of $Nb_2Nb_2Nb_2Ni_6Ni_1$ and $Nb_2Nb_2Nb_2Ni_6Nb_1$) and experimental ΔH_{form} value of μ-Nb_7Ni_6 (-22.6 kJ/mol-atom) is 2.04 kJ/mol-atom at 0 K (and 2.19 kJ/mol-atom at room temperature), which is within the reported error (6.82 kJ/mol-atom) measured by Argent et al. [29] using the calorimetry for six measurements at 50 at. % Nb.

Fig. 7 shows the predicted phonon DOS curves of BCC-Nb, FM FCC-Ni, δ-$NbNi_3$ ($Ni_1Nb_1Ni_2$), and μ-Nb_7Ni_6 ($Nb_2Nb_2Nb_2Ni_6Ni_1$) at their equilibrium volumes at 0 K. The phonon DOS's of BCC-Nb and FCC-Ni show a good agreement with experimental data [75] as shown in Supplemental Materials Fig. S1. Fig. 7 shows that BCC-Nb exhibits a higher phonon DOS at the lowest frequency region (e.g., < 5 THz) compared with those from FCC-Ni, μ-Nb_7Ni_6, and δ-

$NbNi_3$; indicating phonon of BCC-Nb has a larger contribution to Helmholtz energy due to vibrational entropy (see Eq. 3 also the discussion in ref. [76]). The phonon DOS of μ-Nb_7Ni_6 is higher at the highest frequency region (e.g., > 8 THz) with a smaller contribution to vibrational entropy [76]. This trend is in accordance with bulk moduli predicted from DFT and observed from experiments [72,73], i.e., the higher the bulk modulus, the smaller the contribution to entropy, for example, B_0= 173.5 GPa of BCC-Nb and B_0= 207.7 GPa of δ-$NbNi_3$; see Table 5.

5.2. Thermodynamic modeling by ESPEI/PyCalphad

The present model parameters are summarized in the thermodynamic database (TDB) file in the Supplemental Material. ΔH_{form} values calculated from the present CALPHAD modeling are plotted in Fig. 1 together with available experimental data and DFT-based calculations from both the present work and those in the literature [29,36,46,47] The difference with respect to the measurements by Argent et al. [29] is about 2.33 kJ/mol-atom in the composition range of 12.2 – 75.0 at. % Nb, which is lower than the experimental error of 4 kJ/mol-atom by Argent et al. [29]. However, their six measurements at 50 at. % Nb show a difference of 6.8 kJ/mol-atom with the mean value of 22.4 kJ/mol-atom, causing a 6.5 kJ/mol-atom difference in ΔH_{form} with the calculated value of -29.0 kJ/mol-atom at 50 at. % Nb. The measurements by Sokolvskaya et al. [36] were not included in the present CALPHAD modeling since their ΔH_{form} value of -41.6 kJ/mol-atom at 50 at. % Nb is 19.2 kJ/mol-atom more negative than -22.4 kJ/mol-atom by Argent et al. [29]. As mentioned in Section 3.2, the measurements by Alekseev et al. [46] and Lyakishev et al. [47] show large discrepancies (around 8 kJ/mole-atom at 25.0 at. % Nb), which are not considered in the present CAPHAD modeling.

Fig. 2 plots the calculated ΔH_{mix} of liquid at 1900 K from the present CALPHAD modeling and Chen et al.'s modeling [17] in comparison with experiments data by Schaefers et al. [35] at 1927 K and 2000 K, by Chistyakov et al. [34] at 1823 K, by Sudavtsova et al. [36] at 1875 K and AIMD simulations results at 2700K from the present work. It is seen that the present CALPHAD results are in good agreement with (i) those by Chistyakov et al. [34] and Sudavtsova et al. [36] with a mean absolute error (MAE) less than 1.0 kJ/mol-atom (difference of 0.58 kJ/mol-atom with respect to data by Chistyakov et al. [34], and 0.98 kJ/mol-atom with respect to data by Sudavtsova et al. [36]) and (ii) those of AIMD simulations with a MEA of 1.7 kJ/mol-atom. As mentioned in Sec. 3.2, the present CALPHAD modeling excluded the data by Schaefers et al. [35].

Fig. 3 plots the convex hull of ΔH_{form} for both μ-Nb_7Ni_6 (a) and δ-$NbNi_3$ (b) from DFT and two ML predictions (by Alignn [61] and SIPFENN [62]). The results from ML show a good agreement with the results from DFT. Alignn [61] predicted 5 out of 6 configurations (by missing one configuration) of μ-Nb_7Ni_6 and 4 out of 4 configurations of δ-$NbNi_3$ on the convex hull in comparison with DFT calculations, while SIPFENN [62] predicted 3 out of 6 configurations of μ-Nb_7Ni_6 and 3 out of 4 configurations of δ-$NbNi_3$ on the convex hull. By examining the convex hull, SIPFENN [62] gives a maximum difference of 14.22 kJ/mol-atom at 23.0 at. % Nb in μ-Nb_7Ni_6 and 8.79 kJ/mol-atom at 100.0 at. % Nb comparing with DFT results. For Alignn [61], the maximum difference is 10.64 kJ/mol-atom at 92.3 at. % Nb in μ-Nb_7Ni_6 and 9.00 kJ/mol-atom at 50.0 at. % Nb. Detailed comparisons between all configurations from DFT, SIPFENN [62], and Alignn [61] are given in the Supplemental Material. The ML results show a great potential to find the stable configurations and reasonable predictions of ΔH_{form} for each phase, reducing computational efforts by DFT-based calculations.

Table 7 summarizes the calculated invariant reactions from the present CALPHAD modeling and Chen et al.'s modeling [17]. The present modeling shows a good agreement with experiments [27,42] with the difference in compositions less than 4.7 at. % Nb, and the variance of the reaction temperature is less than 10 K. While Chen et al.'s modeling [17] shows the difference in compositions up to 4.8 at. % Nb, with the reaction temperature is less than 10 K compared with experiments [27,42]. For example, in the peritectic reaction from liquid + BCC to form μ-Nb_7Ni_6, the reaction compositions are 50.0 at. % Nb for liquid, 95.5 at. % Nb for FCC, and 54 at. % Nb for μ-Nb_7Ni_6; and the reaction temperatures are 1568 K and 1577 K from experiments [27,28]. From the present CALPHAD predictions, these values are 50.8 at. % Nb, 95.9 at. % Nb, 58.7 at. % Nb, and 1561 K, respectively, compared with 53.0 at. % Nb, 95.3 at. % Nb, 58.8 at. % Nb, and 1563 K from Chen et al.'s modeling work [17]. Notably the present modeling work shows less composition difference (around 2.1 at. % Nb), while Chen et al.'s work [17] shows less temperature difference (2 K), in comparison with the experiments [27,42].

Fig. 8 (a) plots the calculated phase diagram from the present CALPHAD modeling with experimental data superimposed [19,20,25–27,29,35–38,40,42]. The present phase boundaries of δ-$NbNi_3$ between FCC and δ-$NbNi_3$ are predicted from 23.6 to 23.7 at. % Nb at 1070 K – 1420 K, matching well with experimental data around 23.5 at. % Nb at 1323 K from Chen et al. [28], 23.6 at. % Nb at 1280 K from Joubert et al. [21], 23.6 – 23.6 at. % Nb at 1273 K - 1420K from Duerden et al. [27], and 24.1 – 24.1 at. % Nb from 1070 - 1240 K from Murametsu et al. [26]. The calculated phase compositions of δ-$NbNi_3$ from the μ-Nb_7Ni_6 + δ-$NbNi_3$ two-phase equilibrium are from 25.9 to 27.1 at. % Nb at 1170 K – 1420 K, agreeing well with experimental data about 25.6 at. % Nb at 1323 K [28], 26.5 to 26.6 at. % Nb at 1273 K – 1420 K [27], and 26.5 at. % Nb at 1170 K [26]. The calculated compositions of μ-Nb_7Ni_6 from the μ-Nb_7Ni_6 + BCC two-phase equilibrium are 57.3 – 58.1 at. % Nb at 1070 K -1323 K, matching well with experimental data of 56.3 at. % Nb at 1323 K [28], 56.2 – 56.2 at. % Nb at 1070 - 1240 K [26], 58.2 – 58.2 at. % Nb at 1074 -1276 K [44], and 56.9 at. % Nb at 1273 K [20], with the difference less than 1.1 at. % Nb. The 54.0 at. % Nb at 1273 K from Duerden et al. [27] shows large difference (4 at. % Nb) with respect to other experiments [20,26,28,44], which cause the large difference from Duerden et al. [27] compared with the present modeling work.

The comparison of phase diagrams between the present modeling and the previous modeling by Chen et al. [17] is shown in Fig. 8 (b). Phase boundaries between liquid and BCC measured by Wicker et al. [30] were substantially different from those by Duerden et al. [27]. In the present work, both data sets are considered but a lower weight are given to the data from Wicker et al. [30] according to the discussion in Section 3.1. The phase boundaries between liquid and BCC from the present work are around 100 K lower than those by Chen et al. [17] at 70.0 – 85.0 at. % Nb, which give a better match (with an average difference of around 150 K) with the experimental data from Wicker et al. [30] and agree well with the measured data (with an average difference of around 50 K) by Duerden et al. [27] especially at 50.0 – 70.0 at. % Nb. The presently calculated phase compositions of μ-Nb_7Ni_6 in the μ-Nb_7Ni_6 + δ-$NbNi_3$ two-phase region are 48.0 – 48.4 at. % Nb at 1000 K – 1494 K, agreeing with experimental data of 48.6 at. % Nb at 1240 K from Murametsu et al. [26], 49.7 at. % Nb at 1273 K from Svechnikov et al. [44], and 49.5 at. % Nb at

1273 K from Chen et al. [28], while the region are 51.6 – 51.7 at. % Nb at 1000 K – 1458 K by Chen et al. [17]. Even though the calculated phase composition of μ-Nb_7Ni_6 in the μ-Nb_7Ni_6 + δ-$NbNi_3$ two-phase region at 1074 K from the model by Chen et al. [17] is 51.6 at. % Nb, agreeing with the experimental value of 51.8 at. % Nb by Svechnikov et al. [44], the calculated phase composition of μ-Nb_7Ni_6 in the μ-Nb_7Ni_6 + BCC two-phase region at 1074 K by Chen et al. [17] is 54.4 at. % Nb, which is much lower than the experimental value of 58.2 at. % Nb by Svechnikov et al. [44] in comparison with the value of 57.3 at. % Nb from the present work. The present model also reproduces experimental compositions of μ-Nb_7Ni_6 in the μ-Nb_7Ni_6 + BCC two-phase region (57.3 – 58.1 at. % Nb at 1070 K -1323 K), which are much better than those predicted by the model of Chen et al. [17] (54.4 – 56.3 at. % Nb from 1070 – 1323 K), in comparison with experiments by Murametsu et al. [26] (56.2 at. % Nb at 1170 K and 1240 K), Svechnikov et al. [44] (58.2 at. % Nb at 1073 K and 1273 K), and Chen et al. [28] (56.3 at. % Nb at 1273K). For the composition of FCC phase in the FCC + δ-$NbNi_3$ two-phase region, the present modeling work predicts 9.8 – 12.9 at. % Nb at 1070 K -1473 K, while it predicted 7.4 – 11.0 at. % Nb at 1070 K -1473 K by Chen et al. [17]. The present modeling shows a better match with experiments (9.1 at. % Nb at 1070 K) by Guseva [38], while the modeling work by Chen et al. [17] shows a better match with experiments by Pogodin et al. [37] (7.2 at. % Nb at 1173 K).

Fig. 9 shows the calculated site occupancy of Nb in μ-Nb_7Ni_6 from the present work and the work from Dupin et al. [77] in comparison with experimental data by Joubert et al. [20] with an absolute error of less than 0.062 (see Table 8) from the present work, while the error from Chen et al. [17]'s model is up to 0.128 and the error from Joubert et al. model [21] is up to 0.068. Chen et al.'s model [17] only had Nb to occupy the sites $6c_2$ and $6c_3$, therefore, the sites $6c_2$ and $6c_3$ have the same site occupancy values, causing the mean absolute error (MAE) with experiments [20] up to 0.044 in site $6c_2$ which is much higher than that from the present model (0.008 in site $6c_2$). Similarly, the Joubert et al. model [21] had the same MAE value due to only Nb in the sites $6c_2$ and $6c_3$. At the same time, the MAE values compared with experiments are 0.128 at site $6c_1$, 0.032 at site $6c_3$, 0.088 at site 18h, and 0.086 at site 3a by Chen et al. [17] modeling, and 0.58, 0.032, 0.056 and 0.068 by Joubert et al. model [21], respectively. The MAE values from the present model are 0.008 at site $6c_1$, 0.036 at site $6c_2$, 0.032 at site $6c_3$, 0.024 at site 18h, and 0.0016 at site 3a, respectively. Dupin et al. [77] utilized first-principles results during the work to model the site occupancy of Nb in μ -Nb_7Ni_6. In Fig. 9, it can be seen that the site occupancy of Nb at Wyckoff site $6c_3$ is in good agreement with experimental data measured by Joubert et al. [20]. However, there is a discrepancy between the site occupancy of Nb at sites 3a and 18h and experimental data, especially at 49.6 at. % Nb, where both sites show a difference around 0.1. Furthermore, the site occupancy of Nb at sites $6c_1$ and $6c_2$ by Dupin et al. [77] is 1.0 from 49.6 at. % Nb to 56.9 at. % Nb, showing a difference around 0.2 for site $6c_1$ and 0.1 for site $6c_2$ comparing with experimental data. Therefore, the present sublattice models based on Wyckoff sites of μ-Nb_7Ni_6 and δ-$NbNi_3$ and the new function implemented in ESPEI to consider site occupancy data enable better modeling of properties of these two TCP phases.

Fig. 10 shows the 95 % credible interval uncertainty propagation regions of site occupancy of each Wyckoff site concerning Nb in μ-Nb_7Ni_6 predicted by all 56 walkers for the last 10 MCMC iterations during CALPHAD modeling by ESPEI. This region represents the model's confidence of site fraction, showing a good agreement with the uncertainty of experimental data [20]. It is seen that the uncertainty range of Nb in the first sublattice is around 0.2, corresponding to Wyckoff position $6c_1$. The shadow region in Fig. 10 (a) covers 6 out 6 experimental data [20] ,which means the uncertainty of site occupancy at site $6c_1$ includes the uncertainty of experiments. Similarly, at the second, fourth, and fifth sublattices (corresponding to Wyckoff positions $6c_2$, 18h, and 3a, respectively), the uncertainty ranges of Nb are 0.15, 0.05, 0.3, which also covers most experimental data. The only exception is the one at 49.6 at. % Nb at 18h site that has 0.06 difference with respect to the data point at 51.8 at. % Nb, which is large than the average difference (0.03) showing large fluctuation from experiments. For the third sublattice corresponding to Wyckoff position $6c_3$, the uncertainty ranges of Nb do not appear due to the third sublattice of the stable endmembers occupied by Nb around 49.6 -56.9 at. % Nb. The uncertainty propagation regions of site occupancy of Nb in μ-Nb_7Ni_6 cover 22 out of 25 total experimental data, which shows a good match with experimental data considering that the standard deviation of experimental data is around 0.35. The good agreement between uncertainty propagation regions and the experimental data shows that the uncertainty during CALPHAD modeling reflects the uncertainty of experiments.

Fig. 11 provides the uncertainty of the eutectic reactions from the last 10 MCMC iterations. The 68% and 95% are chosen based on empirical rule to show the confidence of the eutectic location [71]. The uncertainty of eutectic reactions of δ-$NbNi_3$ + liquid → μ-Nb_7Ni_6 are plotted in Fig. 11 (a), showing that 68% of the invariant samples have x_{Nb} from 34.7 to 47.6 at. % Nb for liquid phase with temperatures between 1300 to 1615 K. The experiment data (x_{Nb} = 40.5 at. % Nb at 1448 K) [27] are covered in the 68% uncertainty intervals. Similarly, Fig. 11 (b) displays the composition of μ-Nb_7Ni_6 from the peritectic reaction of liquid + μ-Nb_7Ni_6 → BCC, which indicates that 68% of the invariant samples have x_{Nb} from 52.3 to 57.9 at. % Nb in the temperature range from 1240 to 1663 K. The data from experiments (x_{Nb} = 54.0 at. % Nb at 1568 K) [27] are included in the 68% uncertainty intervals.

As another example, Fig. 12 shows the uncertainty propagation regions of ΔH_{mix} in liquid with a 95 % credible interval for all 56 walkers in the last 10 MCMC iterations, indicating that the uncertainty increases in composition range of 0.0 – 40.0 at. % Nb and decreases in 40.0 – 100.0 at. % Nb, with the largest uncertainty around 10 kJ/mol-atom at 30.0 at. % Nb. The uncertainty covers all 13 experimental data points and 4 AIMD data points. It shows that a large increase of ΔH_{mix} uncertainty of liquid appears at the 30.0 at. % Nb region due to the uncertainties (e.g., 5 kJ/mol-atom at 20.0 at. % Nb) in both experiments [34,36] and AIMD data, which are used in the present CALPHAD modeling.

6. Conclusions

The present work combines thermodynamic data from DFT-based first-principles, phonon, and AIMD simulations and ML models, and experiments to remodel Gibbs energy expressions of five phases in the Nb-Ni system. The present focuses are new sublattice models of the TCP phases and the uncertainty quantifications of model parameters and model predictions. The key conclusions are summarized as follows

- New capability is implemented into PyCalphad and ESPEI to use site occupancy data as input to model Gibbs energy parameters.
- The present thermodynamic models of the δ-$NbNi_3$ and μ-Nb_7Ni_6 phases are based on their Wyckoff positions (a three-sublattice model for δ-$NbNi_3$ and a five-sublattice model for μ-

Nb_7Ni_6), providing better descriptions for the TCP phases in comparison with available experimental data in terms of both phase boundaries and site occupancies.

- First-principles as well as phonon calculations are used to predict thermochemical properties of all endmembers of δ-$NbNi_3$ and μ-Nb_7Ni_6 as a function of temperature, providing input data for CALPHAD modeling and compared with predictions with ML models.
- AIMD simulations are used to predict the enthalpy of mixing of liquid phase, supporting the present selection of data from two sets of conflicting experimental data.
- UQ is performed for model parameters and various calculated thermodynamic, site occupancy, and phase equilibrium properties. Particularly, the UQ of site occupancy of Nb in μ-Nb_7Ni_6 reflects well the scattering of experimental data [20].

Acknowledgments:

The authors acknowledge the financial support by the Office of Naval Research (ONR) under Contract No. N00014-21-1-2608 and National Science Foundation (NSF) via Award Nos. CMMI-2050069 and FAIN-2229690. First-principles calculations were performed partially on the Roar supercomputer at the Pennsylvania State University's Institute for Computational and Data Sciences (ICDS), partially on the resources of the National Energy Research Scientific Computing Center (NERSC) supported by the U.S. DOE Office of Science User Facility operated under Contract No. DE-AC02-05CH11231, and partially on the resources of the Extreme Science and Engineering Discovery Environment (XSEDE) supported by NSF with Grant No. ACI-1548562. Part of present work was performed under the auspices of the U.S. DOE at Lawrence Livermore National Laboratory under Contract No. DE-AC52–07NA27344.

Table 1: Wyckoff positions of δ-$NbNi_3$ and μ-Nb_7Ni_6 phases.

Wyckoff position of δ [a]	x	y	z
2a	0	0	0.318
2b	0	0.5	0.651
4f	0.75	0	0.841
Wyckoff position of μ [b]			
3a	0	0	0
6c (1)	0	0	0.167
6c (2)	0	0	0.346
6c (3)	0	0	0.448
18h	0.5	0.5	0.590

[a] δ with space group Pmmn (no. 59), Pearson symbol oP8, Strukturbericht designation $D0_a$, and prototype of β-Cu_3Ti [11].

[b] μ with space group $R\bar{3}m$ (no. 166), Pearson symbol hR13, Strukturbericht designation $D8_5$, and prototype of Fe_7W_6 [12].

Table 2: Sublattice models for δ-$NbNi_3$ and μ-Nb_7Ni_6 used in the previous CALPHAD modeling.

References	Model for δ-$NbNi_3$	Model for μ-Nb_7Ni_6
Kaufman and Nesor [15]	$(Ni)_{0.75}$ $(Nb)_{0.25}$	$(Ni)_{0.47}$ $(Nb)_{0.53}$
Zeng et al. [18]	$(Nb, Ni)_3$ $(Nb, Ni)_1$	$(Nb, Ni)_1Ni_4(Nb, Ni)_2Nb_6$
Bolcavage and Kattner [16]	$(Nb, Ni)_3$ $(Nb, Ni)_1$	$(Nb, Ni)_7$ $(Nb)_6$
Joubert et al. [21]	$(Nb, Ni)_3$ $(Nb, Ni)_1$	$(Nb, Ni)_1Nb_2Nb_2(Nb, Ni)_2(Nb, Ni)_6$
Chen et al. [17]	$(Nb, Ni)_3$ $(Nb, Ni)_1$	$(Nb, Ni)_1Nb_4(Nb, Ni)_2(Nb, Ni)_6$
Zhou et al. [19]	$(Nb, Ni)_3$ $(Nb, Ni)_1$	$(Nb, Ni)_1Nb_4(Nb, Ni)_2(Nb, Ni)_6$

Table 3: Crystallographic information of the phases and their sublattice models used in the present CALPHAD modeling.

Phase name	Strukturbericht	Space group	Pearson symbol	Model
Liquid (L)				(Nb, Ni)
FCC	A1	$Fm\overline{3}m$	cF4	$(Nb, Ni)_1\ (Va)_1$
HCP	A3	$P6_3/mmc$	hP2	$(Nb, Ni)_1\ (Va)_1$
BCC_A2	A2	Im3m	cl2	$(Nb, Ni)_1\ (Va)_3$
δ-$NbNi_3$	$D0_a$	Pmmn	oP8	$(Nb, Ni)_1(Nb, Ni)_1(Nb, Ni)_2$
μ-Nb_7Ni_6	$D8_5$	$R\overline{3}m$	hR13	$(Nb, Ni)_1(Nb, Ni)_2(Nb, Ni)_2(Nb, Ni)_2(Nb, Ni)_6$
$NbNi_8$				$(Nb)_1(Ni)_8$

Table 4: Details of DFT-based first-principles, phonon calculations, and AIMD for each compound or element, including total atom(s) in the cell for the calculations, *k*-points meshes for structure relaxations and the final static calculations (indicated by DFT), supercell sizes for phonon calculations, *k*-points meshes for phonon calculations, and *k*-points meshes for AIMD calculations.

Compounds	Atoms in the cells	*k*-points for DFT	Supercell for phonon	*k*-points for phonon	*k*-points for AIMD
Liquid (L)	108	N/A	N/A	N/A	1×1×1
FCC-Ni	4	23×23×23	2×2×2	6×6×6	N/A
BCC-Nb	2	29×29×29	3×3×3	7×7×7	N/A
δ-$NbNi_3$	8	8×8×7	2×2×2	2×2×2	N/A
μ-Nb_7Ni_6	39	5×5×1	2×2×1	1×1×1	N/A

Table 5: Predicted equilibrium volume (V_0, Å^3/atom), bulk modulus B_0 (GPa), and the derivative of bulk modulus B'_0 from the present EOS fitted to DFT-based calculations at 0 K in comparison with experimental data [11,12,72,73].

Phase	V_0 (Å^3/atom)	% Diff [a]	B_0 (GPa)	% Diff [b]	B'_0	Source
BCC-Nb	18.338	0.224	173.5	0.980	3.86	This work
	18.297		171.8			Expt. [72]
FCC-Ni	21.860	0.243	195.9	5.05	4.81	This work
	21.807		186.0			Expt. [73]
δ-$NbNi_3$	24.176	1.717	207.7		4.65	This work
	24.591					Expt. [11]
μ-Nb_7Ni_6	21.135	0.960	200.0		4.48	This work
	21.338					Expt. [12]

[a, b] Difference between the experimental and the present predicted equilibrium volumes and bulk moduli.

Table 6: ΔH_{form} values of δ-$NbNi_3$ and μ-Nb_7Ni_6 from the present DFT-based calculations at both 0 K and room temperature (RT) from phonon calculations compared with experimental data at RT [29].

Phase	x_{Nb}	ΔH_{form} at RT (kJ/mol-atom)	Diff [b] (kJ/mol-atom)	Source
δ-$NbNi_3$	0.25	-28.51 (-28.38 [a])	3.20 (3.33 [b])	This work
	0.25	-31.71		Expt. [29]
μ-Nb_7Ni_6	0.46	-20.38 (-20.63 [a])	2.07 (4.82 [b])	This work
	0.53	-20.43 (-20.50 [a])	2.02 (1.95 [b])	This work
	0.50	-22.45		Expt. [29]

[a] The presently predicted ΔH_{form} values at 0 K.

[b] Difference between experimental data at RT and the presently predicted ΔH_{form} values at 0 K.

Table 7: Calculated invariant reactions in the Nb-Ni system from the present CALPHAD modeling and from Chen et al.'s modeling [17] in comparison with available experimental data [27,28,37,42].

Type	Reaction compositions (at. % Nb)					Temperature (K)	Source
Eutectic	Liquid	↔	FCC	+	δ-$NbNi_3$		
	16.2		13.7		23.8	1550	This work
	14.9		12.7		24.1	1557	Chen et al. [17]
	16		12.7		22.6	1555	Expt. [27]
						1558	Expt. [28]
Congruent	Liquid	↔	δ-$NbNi_3$				
	25.0		25.0			1675	This work
	25.0		25.0			1672	Chen et al. [17]
	25.0		25.0			1675	Expt. [27]
						1676	Expt. [37]
						1677	Expt. [28]
Eutectic	Liquid	↔	δ-$NbNi_3$	+	μ-Nb_7Ni_6		
	39.9		27.2		48.4	1459	This work
	41.5		26.5		50	1457	Chen et al. [17]
	40.5		27.5		50	1448	Expt. [27]
						1448	Expt. [37]
						1453	Expt. [28]
Peritectic	Liquid	+	BCC	↔	μ-Nb_7Ni_6		
	50.8		95.9		58.7	1561	This work
	53.0		95.3		58.8	1563	Chen et al.
	50.0		95.5		54.0	1568	Expt. [27]
						1577	Expt. [28]
Peritectic	FCC	+	δ-$NbNi_3$	↔	$NbNi_8$		
	8.39		24.1		11.1	800	This work
	5.2		24.2		11.1	788	Chen et al. [17]
						808	Expt. [42]
						788	Expt. [28]

Table 8. Site occupancies of Nb in μ-Nb_7Ni_6 from the present CALPHAD modeling compared with the modeling works by Chen et al. [17] and Joubert et al. [21] and experimental values [20] with the MAE representing mean absolute error and the STD for standard deviation.

Composition	Type of results	$6c_1$	$6c_2$	$6c_3$	18h	3a
$x_{Nb} = 0.496$	Calc., this work	0.74	0.98	1.00	0.03	0.81
	Calc., Chen et al.	0.91	1.00	1.00	0.00	0.86
	Calc., Joubert et al.	0.76	1.00	1.00	0.03	0.77
	Expt.	0.67	0.85	0.95	0.13	0.74
$x_{Nb} = 0.518$	Calc., this work	0.77	0.99	1.00	0.07	0.81
	Calc., Chen et al.	0.91	1.00	1.00	0.01	0.87
	Calc., Joubert et al.	0.83	1.00	1.00	0.04	0.84
	Expt.	0.89	1.00	0.89	0.07	0.77
$x_{Nb} = 0.530$	Calc., this work	0.79	0.99	1.00	0.09	0.81
	Calc., Chen et al.	0.93	1.00	1.00	0.02	0.88
	Calc., Joubert et al.	0.86	1.00	1.00	0.05	0.86
	Expt.	0.78	0.94	1.00	0.10	0.84
$x_{Nb} = 0.553$	Calc., this work	0.82	1.00	1.00	0.12	0.81
	Calc., Chen et al.	0.94	1.00	1.00	0.03	0.89
	Calc., Joubert et al.	0.91	1.00	1.00	0.08	0.91
	Expt.	0.85	0.99	1.00	0.12	0.81
$x_{Nb} = 0.569$	Calc., this work	0.84	1.00	1.00	0.15	0.81
	Calc., Chen et al.	0.95	1.00	1.00	0.08	0.90
	Calc., Joubert et al.	0.93	1.00	1.00	0.10	0.93
	Expt.	0.81	1.00	1.00	0.16	0.81
	MAE, this work	0.008	0.036	0.032	0.024	0.016
	MAE, Chen et al.	0.128	0.044	0.032	0.088	0.086
	MAE, Joubert et al.	0.058	0.044	0.032	0.056	0.068

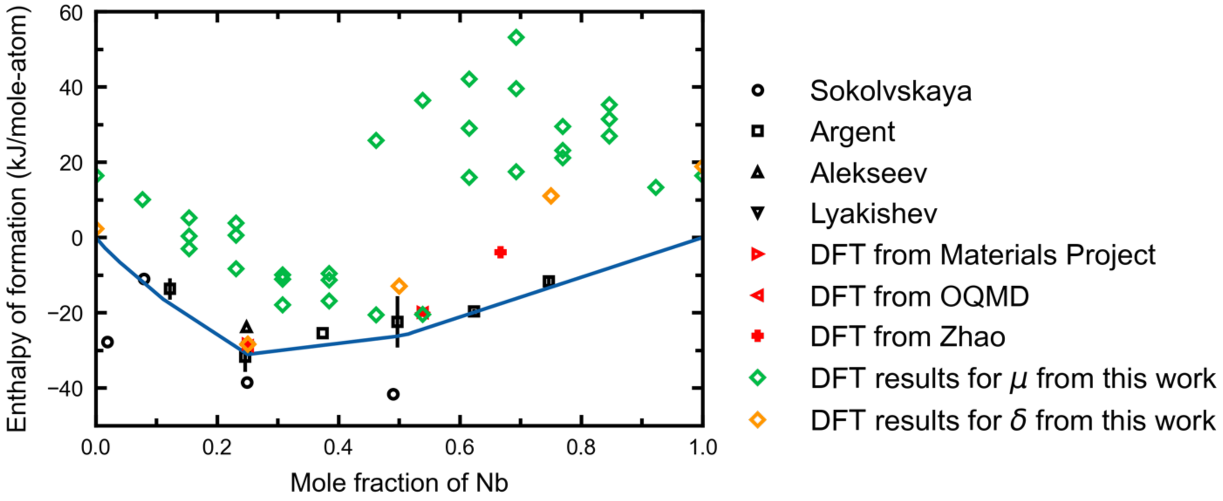

Fig. 1. Predicted enthalpy of formation (from DFT-based calculations (Materials Project, OQMD, DFT calculations from Zhao et al. [43] and the present work) and CALPHAD modeling (Blue line) at 298 K in comparison with experimental data by Argent et al. [29], Sokolvskaya et al. [36], Alekseev et al. [46], and Lyakishev et al. [47]

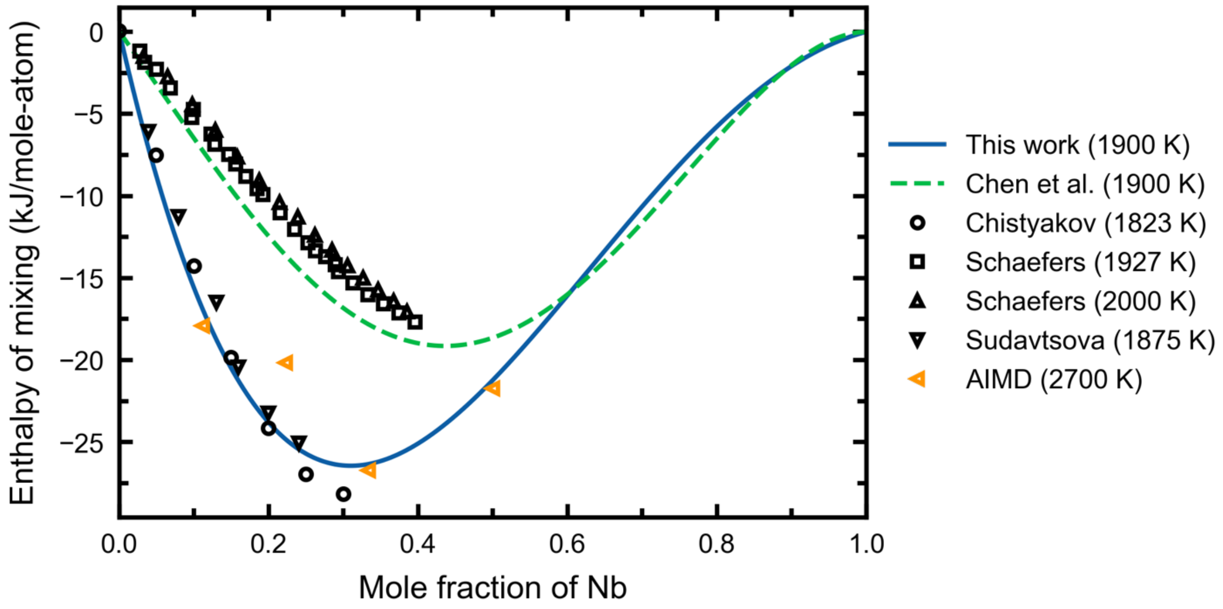

Fig. 2. Calculated ΔH_{mix} values of liquid from CALPHAD-based calculations at 1900 K from the present work (bule line) and Chen et al.'s work [17] in 2006 in comparison with the present AIMD calculations at 2700 K and available experimental data by Schaefers et al. [35] at 1927 K and 2000 K in 1996, by Chistyakov et al. [34] at 1823 K in 1993, and by Sudavtsova et al. [36] at 1875 K in 1998.

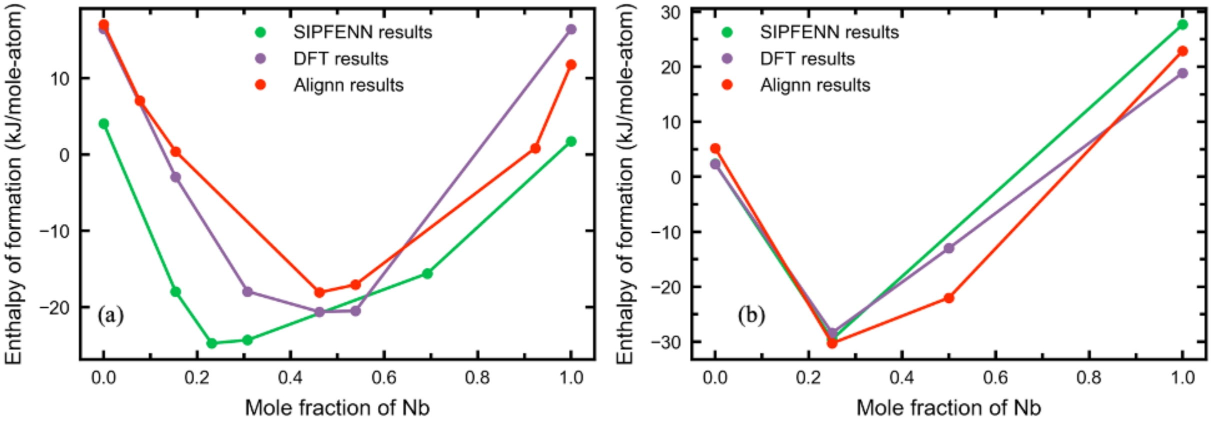

Fig. 3. Calculated convex hulls of ΔH_{form} from the present CALPHAD modeling for (a) μ-Nb_7Ni_6 (b) and δ-$NbNi_3$ by machine learning codes SIPFENN (green line) [62] and Alignn (red line) [61] at 298 K of the Nb-Ni system, in comparison with the present DFT results (purple line) at 0 K.

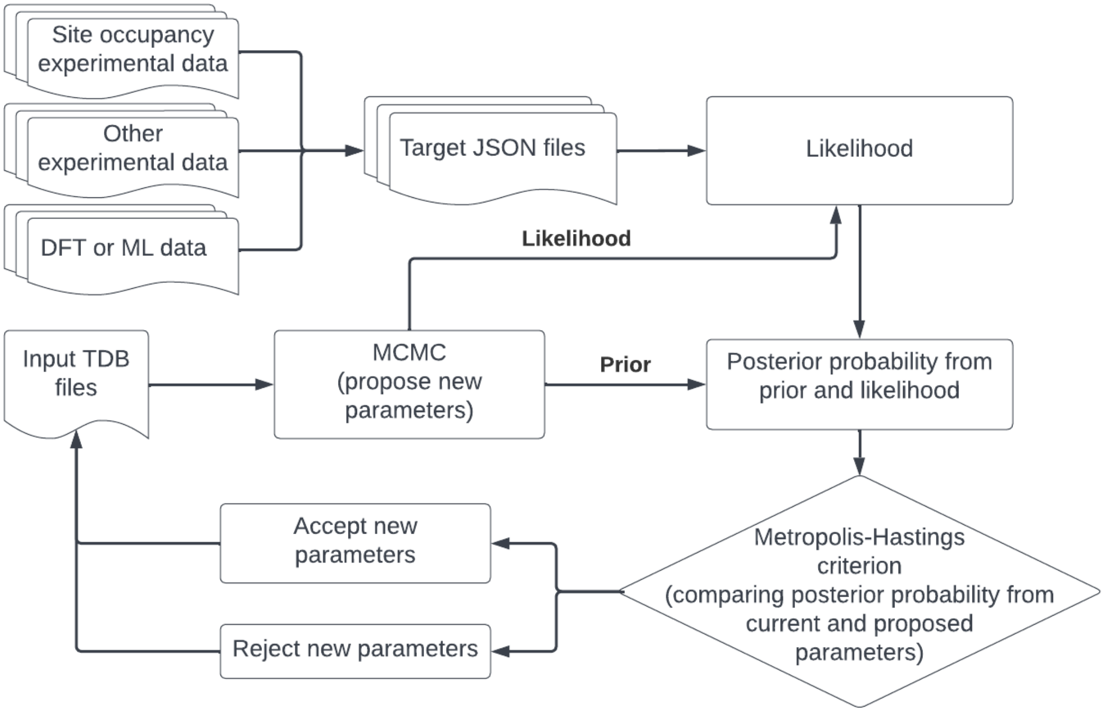

Fig. 4. Workflow of ESPEI implementation to include site occupancy data in CALPHAD modeling. JSON represents the JavaScript Object Notation data format, MCMC the Markov Chain Monte Carlo method, and TDB the thermodynamic database.

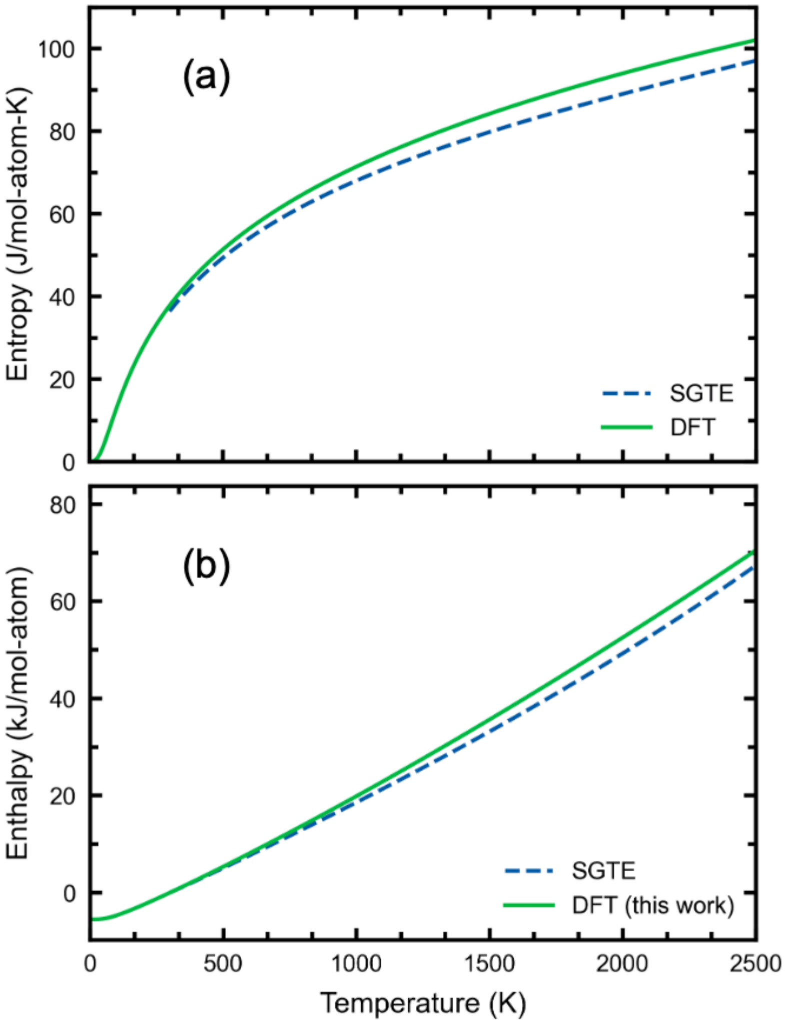

Fig. 5. (a) Entropy and (b) enthalpy of BCC-Nb as a function of temperature predicted by the present phonon calculations using Eq. 2, compared with the results in the SGTE database [66].

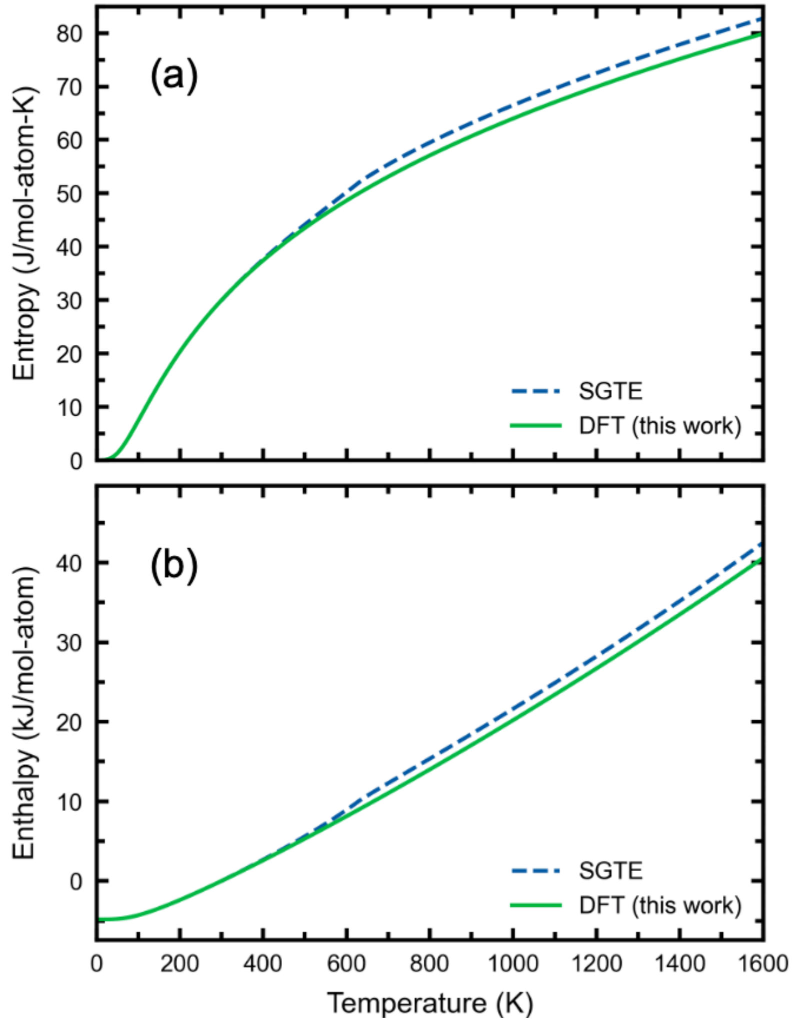

Fig. 6. (a) Entropy and (b) enthalpy of FCC-Ni as a function of temperature predicted by the present phonon calculations using Eq. 2, compared with the results in the SGTE database [66].

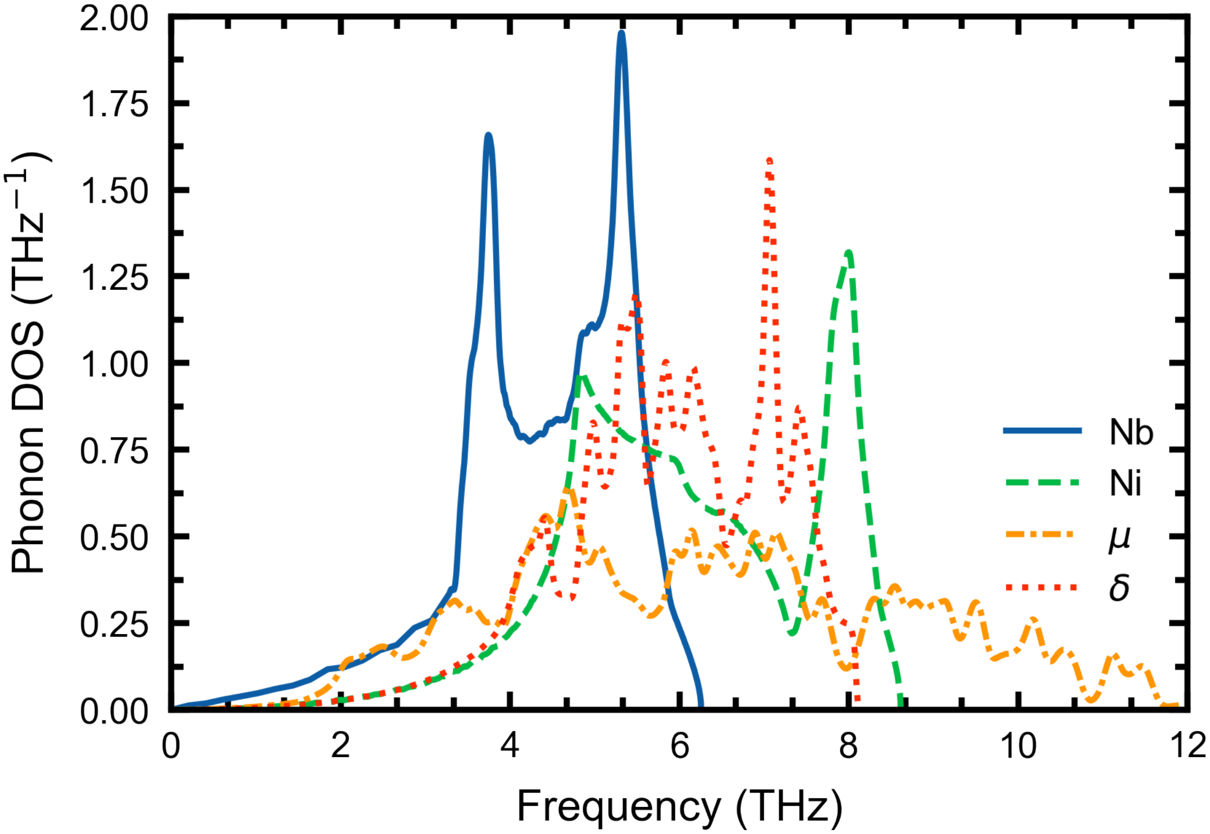

Fig. 7. Predicted phonon density of states (DOS's) at the equilibrium volumes of BCC-Nb, FCC-Ni, δ-$NbNi_3$ ($Ni_1Nb_1Ni_2$), and μ-Nb_7Ni_6 ($Nb_2Nb_2Nb_2Ni_6Ni_1$) from the present DFT-based calculations.

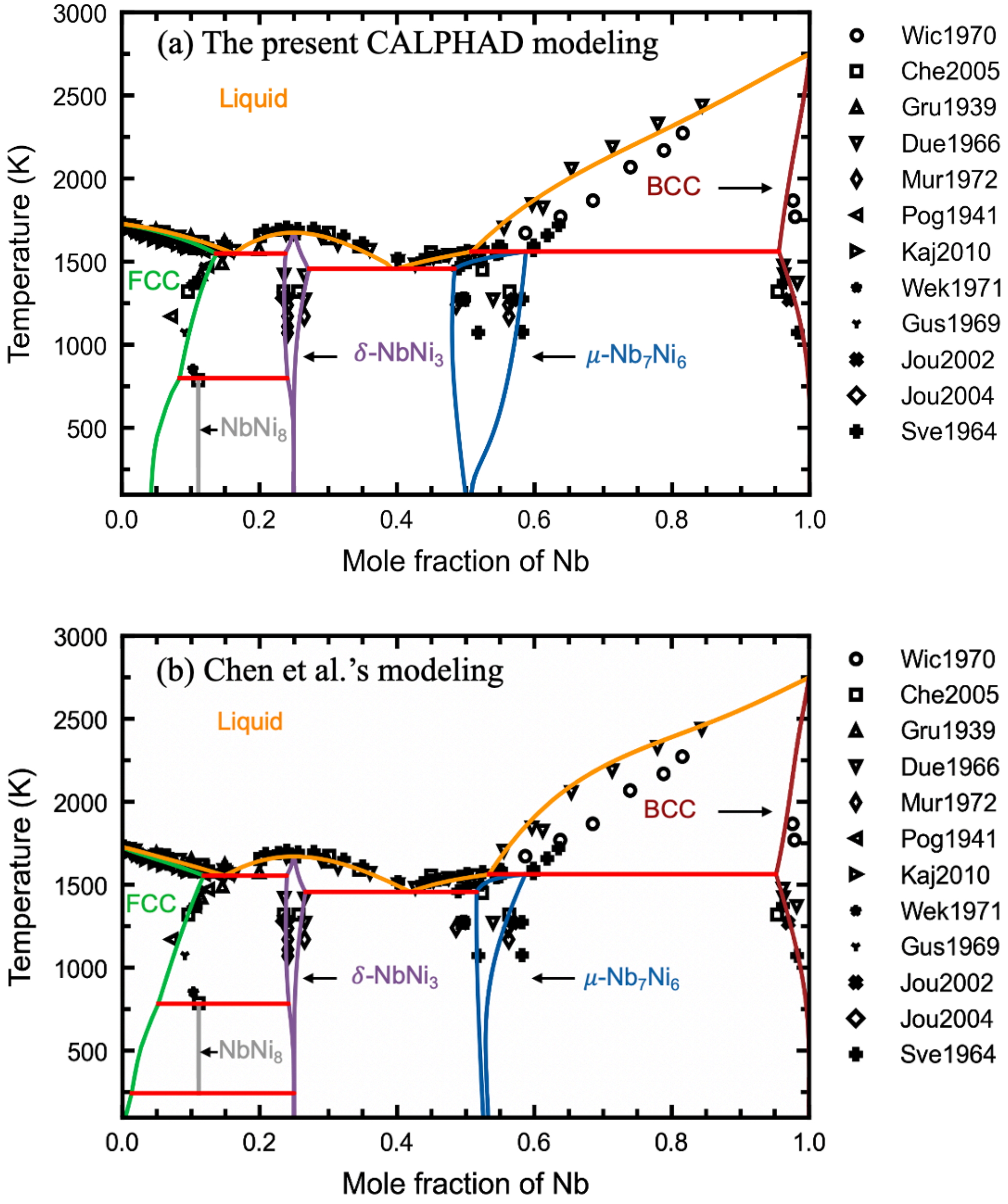

Fig. 8. Calculated phase diagram of the Nb-Ni system from (a) the present CALPHAD modeling and (b) Chen et al.'s modeling [17] compared with available experimental data Joubert et al. [20], Joubert et al. [21], Murametsu et al. [26], Duerden et al. [27], Chen et al. [28], Wicker et al. [30], Pogodin et al.[37], Grube et al. [38], Kajikawa et al. [39], Wekken et al. [42], Svechnikov et al. [44].

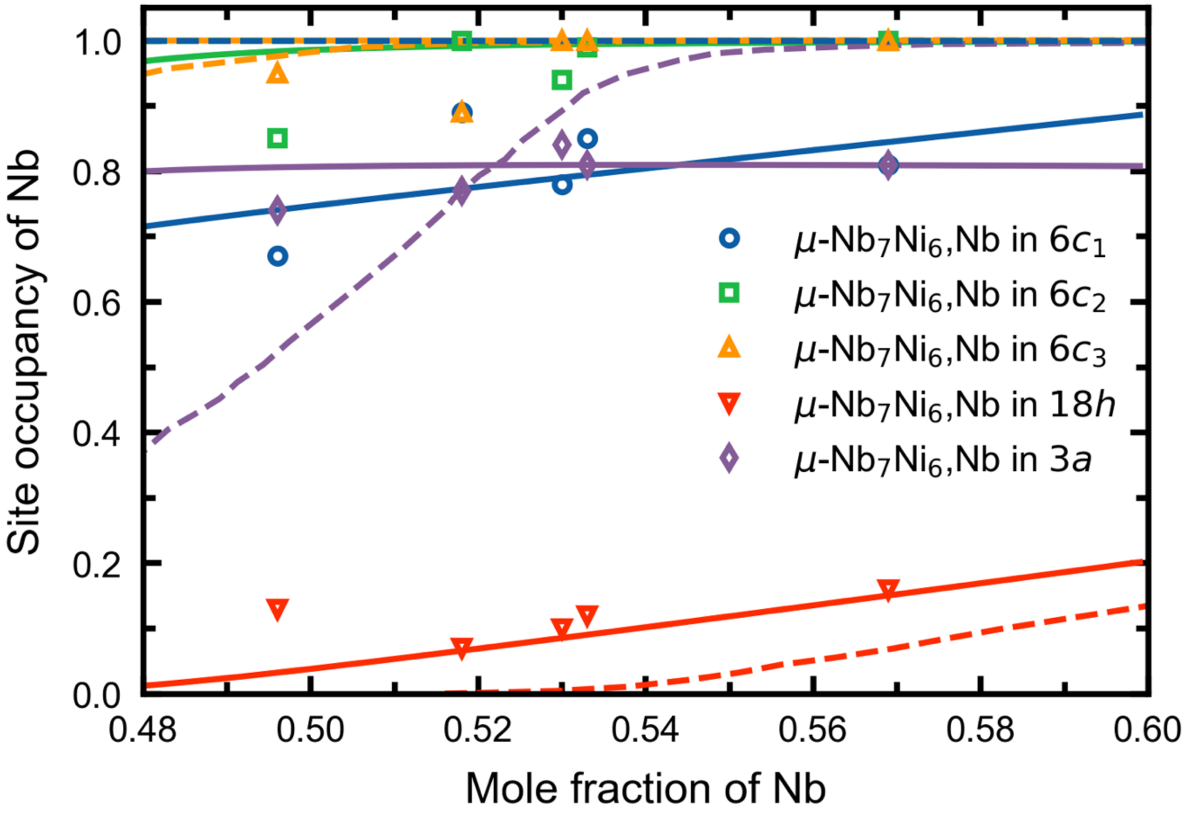

Fig. 9. Calculated site occupancies of Nb in μ-Nb_7Ni_6 at 1273 K from both present work (solid lines) and work from Dupin et al. [77] (dash lines) in comparison with experimental data (symbols) from Joubert et al. [20]; see the values shown in Table 8.

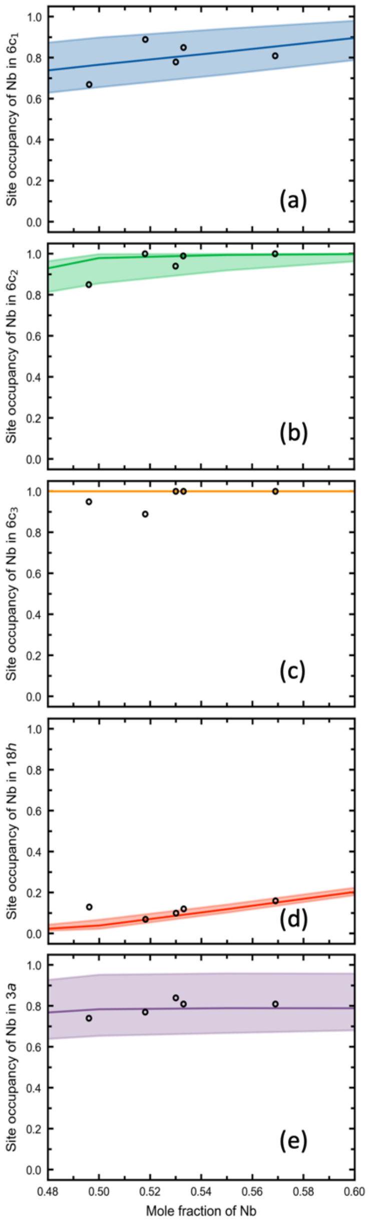

Fig. 10. Uncertainty quantification (shaded region) in 95% uncertainty intervals of site occupancies of Nb in μ-Nb_7Ni_6 at 1273 K (the lines) in comparison with experimental data (symbols) from Joubert et al. [20] for each Wyckoff site: (a) $6c_1$, (b) $6c_2$, (c) $6c_3$, (d) 18h, and (e) 3a.

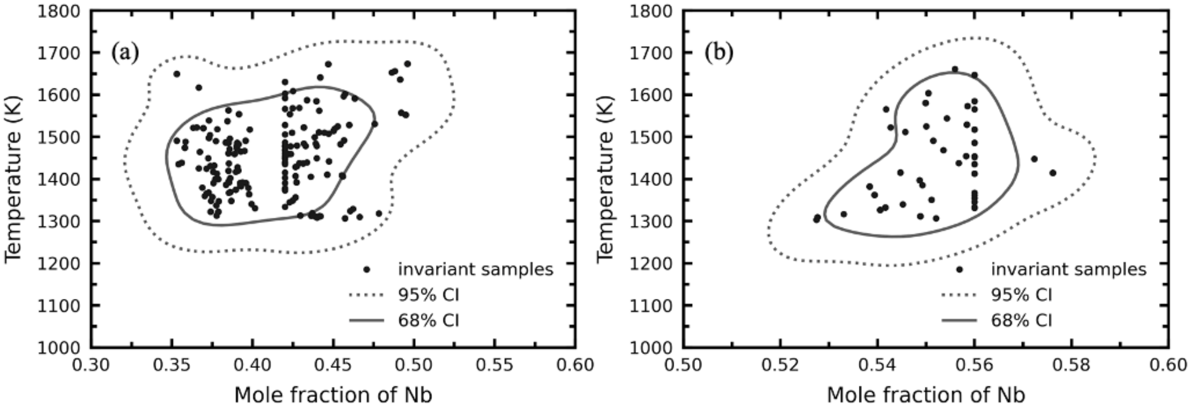

Fig. 11. Uncertainty quantification of liquid phase during δ-$NbNi_3$ + liquid → μ-Nb_7Ni_6 eutectics (a) and μ-Nb_7Ni_6 during liquid + μ-Nb_7Ni_6 → BCC peritectic (b) plotted for last 10 MCMC iterations with 68% and 95% uncertainty intervals, respectively.

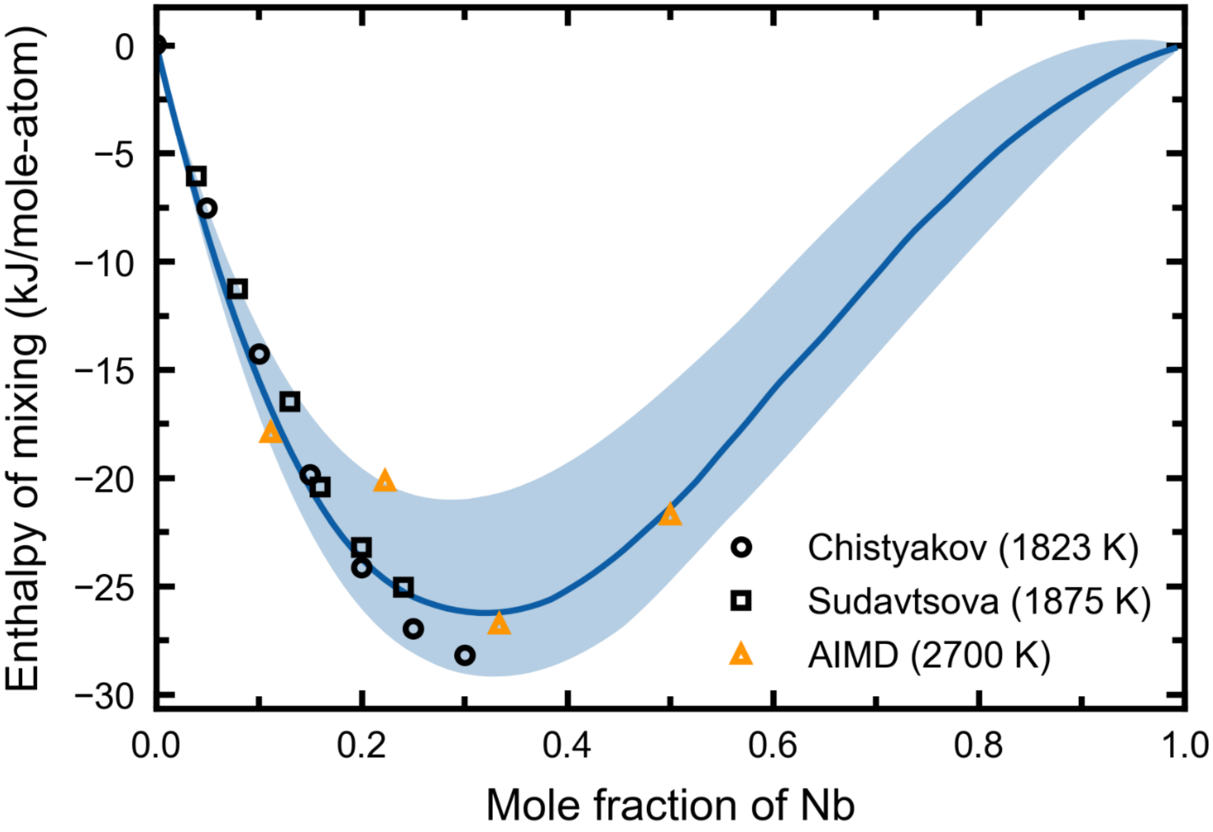

Fig. 12. Uncertainty quantification (shaded region) of the calculated ΔH_{mix} (the line) in the liquid phase at 1900 K in comparison with the present AIMD results at 2700 K and available experimental data by Chistyakov et al. [34] at 1823 K, and by Sudavtsova et al. [36] at 1875 K.

References:

[1] F.C. Frank, J.S. Kasper, Complex alloy structures regarded as sphere packings. I. Definitions and basic principles, Acta Crystallogr. 11 (1958) 184–190. https://doi.org/10.1107/S0365110X58000487.

[2] B. Seiser, R. Drautz, D.G. Pettifor, TCP phase predictions in Ni-based superalloys: Structure maps revisited, Acta Mater. 59 (2011) 749–763. https://doi.org/10.1016/j.actamat.2010.10.013.

[3] T. Sugui, W. Minggang, L. Tang, Q. Benjiang, X. Jun, Influence of TCP phase and its morphology on creep properties of single crystal nickel-based superalloys, Mater. Sci. Eng. A. 527 (2010) 5444–5451. https://doi.org/10.1016/j.msea.2010.05.027.

[4] J.H. Alano, R.L. Siqueira, A.D. de Oliveira, G. dos Santos Vacchi, C.A. Della Rovere, S.E. Kuri, Effect of TCP phase formation on the electrochemical corrosion behavior of the nickel-based superalloy UNS N26455, Corros. Sci. 177 (2020). https://doi.org/10.1016/j.corsci.2020.108965.

[5] P. Pandey, S.K. Makineni, A. Samanta, A. Sharma, S.M. Das, B. Nithin, C. Srivastava, A.K. Singh, D. Raabe, B. Gault, K. Chattopadhyay, Elemental site occupancy in the L12 A3B ordered intermetallic phase in Co-based superalloys and its influence on the microstructure, Acta Mater. 163 (2019) 140–153. https://doi.org/10.1016/j.actamat.2018.09.049.

[6] P. Petrzak, K. Kowalski, M. Blicharski, Analysis of phase transformations in Inconel 625 alloy during annealing, Acta Phys. Pol. A. 130 (2016) 1041–1044. https://doi.org/10.12693/APhysPolA.130.1041.

[7] Y.Q. Mu, C.S. Wang, W.L. Zhou, L.Z. Zhou, Tensile Properties of Cast Alloy IN625 in Relation to δ Phase Precipitation, Acta Metall. Sin. (English Lett. 32 (2019) 535–540. https://doi.org/10.1007/s40195-018-0772-y.

[8] S. Qin, T.C. Novak, M.K. Vailhe, Z.K. Liu, A.M. Beese, Plasticity and fracture behavior of Inconel 625 manufactured by laser powder bed fusion: Comparison between as-built and stress relieved conditions, Mater. Sci. Eng. A. 806 (2021) 140808. https://doi.org/10.1016/j.msea.2021.140808.

[9] H.M. Tawancy, On the Precipitation of Intermetallic Compounds in Selected Solid-Solution-Strengthened Ni-Base Alloys and Their Effects on Mechanical Properties, Metallogr. Microstruct. Anal. 6 (2017) 200–215. https://doi.org/10.1007/s13632-017-0352-y.

[10] Z.K. Liu, First-Principles calculations and CALPHAD modeling of thermodynamics, J. Phase Equilibria Diffus. 30 (2009) 517–534. https://doi.org/10.1007/s11669-009-9570-6.

[11] T. Fang, S.J. Kennedy, L. Quan, T.J. Hicks, The structure and paramagnetism of Ni3Nb, J. Phys. Condens. Matter. 4 (1992) 2405–2414. https://doi.org/10.1088/0953-8984/4/10/007.

[12] P.I. Kripyakevich, E.I. Gladyshevskii, E.N. Pylaeva, Compounds of the W6Fe7 type in the Ta-Ni

and Nb-Ni systems, Sov. Phys. Crystallogr. 7 (1962) 165–168.

[13] Workshop on thermodynamic modelling of solutions and alloys: Schloβ Ringberg, March 10 to March 16, 1996, Calphad. 21 (1997) 171–218. https://doi.org/10.1016/S0364-5916(97)00021-7.

[14] M. Hillert, The compound energy formalism, J. Alloys Compd. 320 (2001) 161–176.

[15] L. Kaufman, H. Nesor, Coupled phase diagrams and thermochemical data for transition metal binary systems—II, Calphad. 2 (1978) 81–108.

[16] A. Bolcavage, A Reassessment of the Calculated Ni-Nb Phase Diagram, J. Phase Equilibria. 17 (1996) 92–100.

[17] H. Chen, Y. Du, Refinement of the thermodynamic modeling of the Nb – Ni system, Calphad. 30 (2006) 308–315. https://doi.org/10.1016/j.calphad.2006.02.005.

[18] Z. Kejun, Z. Xianzhang, J. Zhanpeng, A thermodynamic calculation of the Ni-Nb phase diagram, J. Alloys Compd. 179 (1992) 177–185.

[19] C. Zhou, C. Guo, J. Li, C. Li, Z. Du, Key Experiments and Thermodynamic Description of the Co-Nb-Ni System, Metall. Mater. Trans. A Phys. Metall. Mater. Sci. 51 (2020) 5892–5911. https://doi.org/10.1007/s11661-020-05963-2.

[20] J.-M. Joubert, Y. Feutelais, Contribution of the Rietveld method to non-stoichiometric phase modeling. Part II: α-Tl5Te3 and μ Nb-Ni as experimental examples, Calphad. 26 (2002) 427–438.

[21] J.-M. Joubert, B. Sundman, N. Dupin, Assessment of the niobium–nickel system, Calphad. 28 (2004) 299–306.

[22] B. Bocklund, R. Otis, A. Egorov, A. Obaied, I. Roslyakova, Z.K. Liu, ESPEI for efficient thermodynamic database development, modification, and uncertainty quantification: Application to Cu-Mg, MRS Commun. 9 (2019) 618–627. https://doi.org/10.1557/mrc.2019.59.

[23] ESPEI: Extensible Self-optimizing Phase Equilibria Infrastructure, Https://Espei.Org. (n.d.).

[24] R. Otis, Z.-K. Liu, pycalphad: CALPHAD-based Computational Thermodynamics in Python, J. Open Res. Softw. 5 (2017) 1–11. https://doi.org/10.5334/jors.140.

[25] PyCalphad: Python library for computational thermodynamics using the CALPHAD method, Https://Pycalphad.Org. (n.d.).

[26] Y. Muramatsu, F. Roux, A. Vignes, Influence de la pression sur la croissance des couches des composes intermetalliques dans les couples de diffusion niobium/nickel, Trans. Japan Inst. Met. 16 (1975) 61–72.

[27] I.J. Duerden, W. Hume-Rothery, The equilibrium diagram of the system niobium-nickel, J. Less Common Met. 11 (1966) 381–387.

[28] H. Chen, Y. Du, H. Xu, Y. Liu, J.C. Schuster, Experimental investigation of the Nb-Ni phase diagram, J. Mater. Sci. 40 (2005) 6019–6022. https://doi.org/10.1007/s10853-005-4553-4.

[29] B.B. Argent, B.J. Pearcey, Heats of Formation of Nb−Ni Alloys, Phys. Chem. Met. Solut. Lntermetallic Compd. 31 (1959) 1–6.

[30] A. Wicker, C. Allibert, J. Oriole, E. Bonnier, Phase Equilibrium in Ni− Nb− Mo, Ni− Nb, and Ni−Mo Systems, CR Acad. Sci., Ser. C. 271 (1970) 273–275.

[31] M. Mathon, D. Connétable, B. Sundman, J. Lacaze, Calphad-type assessment of the Fe–Nb–Ni ternary system, Calphad. 33 (2009) 136–161.

[32] L.P. Déo, M.F. de Oliveira, Accuracy of a selection criterion for glass forming ability in the Ni–Nb–Zr system, J. Alloys Compd. 615 (2014) S23–S28.

[33] K. Santhy, K.C.H. Kumar, Thermodynamic reassessment of Nb-Ni-Ti system with order–disorder model, J. Alloys Compd. 619 (2015) 733–747.

[34] L.S. Chistyakov, K.V. Grigorovich, A.Y. Stomakhin, Izv. Vyssh. Uchebn. Zaved., (1993) 83–84.

[35] K. Schaefers, J. Qin, M. Rösner-Kuhn, M.G. Frohberg, Mixing enthalpies of liquid Ni-V, Ni-Nb and Ni-Ta alloys measured by levitation alloying calorimetry, Can. Metall. Q. 35 (1996) 47–51.

[36] E.M. Sokolvskaya, L.L. Mechkov, G.A. Tikhankin, No Title, Dokl. Akad. Nauk SSSR. 229 (1976) 914–916.

[37] S.A. Pogodin, A.N. Selikmann, On the Phase Diagram of the System Nickel-Niobium, in: CR Acad. Sci. URSS, 1941: pp. 895–897.

[38] G. Grube, Uber die gewinnung von festen niob-nickel-legierungen durch reduktion von niobpentosyd be1 gegenwart von nickel., Zeitschrift Für Elektrochemie Und Angew. Phys. Chemie. 367 (1939) 1–4.

[39] K. Kajikawa, K. Oikawa, F. Takahashi, H. Yamada, K. Anzai, Reassessment of liquid/solid equilibrium in Ni-rich side of Ni-Nb and Ni-Ti systems, Mater. Trans. 51 (2010) 781–786. https://doi.org/10.2320/matertrans.M2009351.

[40] L.N. Guseva, R.S. Mints, Y.S. Malkov, PHASE EQUILIBRIA IN THE NI-NI 3 AL-NI 3 NB SYSTEM AT 800-1200 C, IZVEST AKAD Nauk SSSR Met. 5 (1969) 186–190.

[41] W.E. Quist, C.J. van der Wekken, R. Taggart, D.H. Polonis, INTERMEDIATE COMPOUNDS Ni8Nb (Cb) IN NICKEL-RICH NICKEL--NIOBIUM (COLUMBIUM) ALLOYS., Trans. Met. Soc. AIME. 245 (1969) 345–349.

[42] C.J. van der Wekken, R. Taggart, D.H. Polonis, Short-Range Order and the Nucleation of Long-Range Order in Ni-Rich Nickel-Niobium Alloys, Met. Sci. J. 5 (1971) 219–223.

[43] J.F. Zhao, H.P. Wang, B. Wei, A new thermodynamically stable Nb2Ni intermetallic compound phase revealed by peritectoid transition within binary Nb-Ni alloy system, J. Mater. Sci. Technol. 100 (2022) 246–253. https://doi.org/10.1016/j.jmst.2021.07.001.

[44] V.N. Svechnikov, V.M. Pan, V.G. Korobeinikov, CONSTITUTION DIAGRAM OF NIOBIUM

NICKEL ALLOY, Sb. Nauchnykh Tr. Instituta Metallofiz. Akad. Nauk Ukr. SSR (Ukrainian SSR) SR). (1964).

[45] V.S. Sudavtsova, Thermodynamic properties of binary Ni-V (Nb, Ta) melts, Metally. (1998) 44.

[46] G.D. Alekseev, D.M. Khazins, N.A. Kalinina, V. V Kruglov, On the accuracy of spatial position and tension of wire electrodes in proportional chambers, Prib. i Tekhnika Ehksperimenta. (1978) 47–50.

[47] N.P. Lyakishev, Y.U.P. Snitko, V.I. Alekseev, G. Levshin, Determination of the Free Energy of Formation of Ni3Nb Intermetallic, Zh. Fiz. Khim. 57 (1983) 180–182.

[48] A. Jain, S.P. Ong, G. Hautier, W. Chen, W.D. Richards, S. Dacek, S. Cholia, D. Gunter, D. Skinner, G. Ceder, Commentary: The Materials Project: A materials genome approach to accelerating materials innovation, APL Mater. 1 (2013) 11002.

[49] S. Kirklin, J.E. Saal, B. Meredig, A. Thompson, J.W. Doak, M. Aykol, S. Rühl, C. Wolverton, The Open Quantum Materials Database (OQMD): assessing the accuracy of DFT formation energies, Npj Comput. Mater. 1 (2015) 1–15.

[50] S.-L. Shang, Y. Wang, T.J. Anderson, Z.-K. Liu, Achieving accurate energetics beyond (semi-)local density functional theory: Illustrated with transition metal disulfides, Cu2ZnSnS4, and Na3PS4 related semiconductors, Phys. Rev. Mater. 3 (2019) 015401. https://doi.org/10.1103/PhysRevMaterials.3.015401.

[51] A. Kroupa, O. Zobač, K.W. Richter, The thermodynamic reassessment of the binary Al–Cu system, J. Mater. Sci. 56 (2021) 3430–3443. https://doi.org/10.1007/s10853-020-05423-7.

[52] G. Cacciamani, A. Dinsdale, M. Palumbo, A. Pasturel, The Fe-Ni system: Thermodynamic modelling assisted by atomistic calculations, Intermetallics. 18 (2010) 1148–1162. https://doi.org/10.1016/j.intermet.2010.02.026.

[53] S.-L. Shang, Y. Wang, D. Kim, Z.-K. Liu, First-principles thermodynamics from phonon and Debye model: Application to Ni and Ni3Al, Comput. Mater. Sci. 47 (2010) 1040–1048.

[54] Y. Wang, Z.K. Liu, L.Q. Chen, Thermodynamic properties of Al, Ni, NiAl, and Ni3Al from first-principles calculations, Acta Mater. 52 (2004) 2665–2671. https://doi.org/10.1016/j.actamat.2004.02.014.

[55] G. Kresse, J. Furthmuller, J. Furthmüller, J. Furthmueller, J. Furthmuller, J. Furthmüller, J. Furthmü, Efficient iterative schemes for ab initio total-energy calculations using a plane-wave basis set, Phys. Rev. B. 54 (1996) 11169.

[56] P.E. Bloechl, P.E. Blöchl, P.E.E. Blochl, P.E. Blöchl, P.E. Bloechl, P.E. Blöchl, P.E.E. Blochl, P.E. Blöchl, Projector augmented-wave method, Phys. Rev. B. 50 (1994) 17953.

[57] J.P. Perdew, K. Burke, M. Ernzerhof, Generalized gradient approximation made simple, Phys. Rev.

Lett. 77 (1996) 3865.

[58] S. Nosé, A unified formulation of the constant temperature molecular dynamics methods, J. Chem. Phys. 81 (1984) 511–519. https://doi.org/10.1063/1.447334.

[59] Y. Kassir, M. Kupiec, A. Shalom, G. Simchen, Cloning and mapping of CDC40, a Saccharomyces cerevisiae gene with a role in DNA repair, Curr. Genet. 9 (1985) 253–257. https://doi.org/10.1007/BF00419952.

[60] C. Wang, W. Zhong, J.C. Zhao, Insights on phase formation from thermodynamic calculations and machine learning of 2436 experimentally measured high entropy alloys, J. Alloys Compd. 915 (2022) 165173. https://doi.org/10.1016/j.jallcom.2022.165173.

[61] K. Choudhary, B. DeCost, Atomistic Line Graph Neural Network for improved materials property predictions, Npj Comput. Mater. 7 (2021) 1–8. https://doi.org/10.1038/s41524-021-00650-1.

[62] A.M. Krajewski, J.W. Siegel, J. Xu, Z.K. Liu, Extensible Structure-Informed Prediction of Formation Energy with improved accuracy and usability employing neural networks, Comput. Mater. Sci. 208 (2022) 111254. https://doi.org/10.1016/j.commatsci.2022.111254.

[63] J.E. Saal, S. Kirklin, M. Aykol, B. Meredig, C. Wolverton, Materials design and discovery with high-throughput density functional theory: The open quantum materials database (OQMD), Jom. 65 (2013) 1501–1509. https://doi.org/10.1007/s11837-013-0755-4.

[64] K. Choudhary, K.F. Garrity, A.C.E. Reid, B. DeCost, A.J. Biacchi, A.R. Hight Walker, Z. Trautt, J. Hattrick-Simpers, A.G. Kusne, A. Centrone, A. Davydov, J. Jiang, R. Pachter, G. Cheon, E. Reed, A. Agrawal, X. Qian, V. Sharma, H. Zhuang, S. V. Kalinin, B.G. Sumpter, G. Pilania, P. Acar, S. Mandal, K. Haule, D. Vanderbilt, K. Rabe, F. Tavazza, The joint automated repository for various integrated simulations (JARVIS) for data-driven materials design, Npj Comput. Mater. 6 (2020). https://doi.org/10.1038/s41524-020-00440-1.

[65] O. Redlich, A.T. Kister, Algebraic representation of thermodynamic properties and the classification of solutions, Ind. Eng. Chem. 40 (1948) 345–348.

[66] A.T. Dinsdale, SGTE Data for Pure Elements, CALPHAD. 15 (1991) 317–425.

[67] Z.-K. Liu, Y. Wang, Computational thermodynamics of materials, Cambridge University Press, 2016.

[68] D. Foreman-Mackey, D.W. Hogg, D. Lang, J. Goodman, emcee : The MCMC Hammer , Publ. Astron. Soc. Pacific. 125 (2013) 306–312. https://doi.org/10.1086/670067.

[69] J. Goodman, J. Weare, Ensemble samplers with affine invariance, Commun. Appl. Math. Comput. Sci. 5 (2010) 65–80. https://doi.org/10.2140/camcos.2010.5.65.

[70] B.B.P. Carlin, T.A. Louis, Book Reviews, J. Am. Stat. Assoc. 109 (2014) 1325–1337. https://doi.org/10.1080/01621459.2014.963405.

[71] N.H. Paulson, B.J. Bocklund, R.A. Otis, Z.-K. Liu, M. Stan, Quantified Uncertainty in Thermodynamic Modeling for Materials Design, Acta Mater. 174 (2019) 9–15. https://doi.org/10.1016/j.actamat.2019.05.017.

[72] J. Trivisonno, S. Vatanayon, M. Wilt, J. Washick, R. Reifenberger, Temperature dependence of the elastic constants of niobium and lead in the normal and superconducting states, J. Low Temp. Phys. 12 (1973) 153–169. https://doi.org/10.1007/BF00654733.

[73] G. Simmons, H. Wang, A Handbook of Single Crystal Elastic Constants and Calculated Aggregate Properties, (1971).

[74] Y.S. Touloukian, R.K. Kirby, R.E. Taylor, P.D. Desai, Thermal expansion: metallic elements and alloys, (1975).

[75] K.H. Hellwege, J.L. Olsen, Metals: Phonon states, electron states and Fermi surfaces. Subvolume a. Phonon states of elements, electron states and Fermi surfaces of alloys. Metalle: Phononenzustaende, Elektronenzustaende und Fermiflaechen. Teilband a. Phononenzustaende von Elementen, (1981).

[76] S.L. Shang, Y. Wang, D.E. Kim, Z.K. Liu, First-principles thermodynamics from phonon and Debye model: Application to Ni and Ni3Al, Comput. Mater. Sci. 47 (2010) 1040–1048. https://doi.org/10.1016/j.commatsci.2009.12.006.

[77] N. Dupin, S.G. Fries, J.M. Joubert, B. Sundman, M.H.F. Sluiter, Y. Kawazoe, A. Pasturel, Using first-principles results to calculate finite-temperature thermodynamic properties of the Nb-Ni μ phase in the Bragg-Williams approximation, Philos. Mag. 86 (2006) 1631–1641. https://doi.org/10.1080/14786430500437488.